

Electric-field Induced Bistability in Single-Molecule Conductance Measurements for Boron Coordinated Curcuminoid Compounds

Ignacio José Olavarría-Contreras,^{a,†} Alvaro Etcheverry-Berrios,^{b,†} Wenjie Qian,^c Cristian Gutiérrez-Cerón,^d Aldo Campos-Olguín,^b E. Carolina Sañudo,^{e,f} Diana Dulić,^d Eliseo Ruiz,^{e,g} Núria Aliaga-Alcalde,^{c,h,*} Monica Soler^{b,*} and Herre S. J. van der Zant^{a,*}

^a Kavli Institute of Nanoscience, Delft University of Technology, Lorentzweg 1, Delft 2628 CJ, The Netherlands.

^b Departamento de Ingeniería Química, Biotecnología y Materiales, Facultad de Ciencias Físicas y Matemáticas, Universidad de Chile, Beauchef 851, Santiago, Chile.

^c ICMAB-CSIC (Institut de Ciència dels Materials de Barcelona), Campus de la Universitat Autònoma de Barcelona, 08193 Bellaterra, Spain.

^d Departamento de Física, Facultad de Ciencias Físicas y Matemáticas, Universidad de Chile, Santiago, Chile.

^e Departament de Química Inorgànica i Orgànica and Institut de Nanociència i Nanotecnologia, Universitat de Barcelona, Diagonal 645 08028, Barcelona, Spain.

^f Institut de Nanociència i Nanotecnologia, Universitat de Barcelona, Diagonal 645, 08028, Barcelona, Spain.

^g Departament de Química Inorgànica i Orgànica and Institut de Recerca de Química Teòrica i Computacional, Universitat de Barcelona, Diagonal 645, E-08028 Barcelona, Spain.

^h ICREA (Institut Catalana de Recerca i Estudis Avançats), Passeig Lluís Companys, 23, 08018 Barcelona, Spain.

[†] These authors contributed equally

Contents

1. General Information	p. 2 – 3
2. Synthetic procedures	p. 4 – 7
3. Crystallographic data of 1 (Fig. S1, and Tables S1-S3)	p. 8 – 9
4. Crystallographic data of 3 (Fig. S2, and Tables S4-S6)	p. 10 – 11
5. ¹ H, ¹³ C, ¹⁹ F NMR spectra of curcuminoids and dbm derivatives (Figs. S3-S19)	p. 12 – 20
6. FTIR Spectra (Figs. S20-S27)	p. 21 – 24
7. UV-Vis Diffuse Reflectance Spectra (Figs. S28-S35)	p. 25 - 28
8. Cyclic Voltammetry and Differential Pulse Voltammetry (Figs. S36-S44)	p. 29 – 33
9. Stability study in different solvents and temperature by NMR (Figs. S45-S49)	p. 34 – 36
10. MCBJ method (Figs. S50-S54)	p. 37 – 39
11. Theoretical studies (Table S7-S9, Figs. S55-S60)	p. 40 – 44
References	p. 45

1. General Information

Materials and Methods

Experiments were carried out in aerobic conditions, using commercial grade solvents for the synthesis of all the compounds (**1-6**). Synthesis of the (S-(4-formylphenyl) dimethylcarbamothioate) and its precursors (SI) were performed by modifying the methodology described elsewhere.¹ Synthesis of di- μ -hydroxo-bis(N,N,N',N'-tetramethylenediamine)-dicopper(II) perchlorate ([CuOH(TMEDA)]₂(ClO₄)₂) was performed following related literature.² The syntheses of the S-thiocarbamate CCM (S-CCM, **4a**) and the coordination compound, S-CCM-BF₂ (**4**) are described in the SI. ((1E,4Z,6E)-5-hydroxy-1,7-di(thiophen-3-yl)hepta-1,4,6-trien-3-one), described here as (Thph-CCM) was synthesized as previously reported by us.³ Compound **5** was synthesized by the use of the former; the synthetic methodology is described in the SI together with the synthesis of the free ligand MeS-dbm (**6a**) and related coordination compound, MeS-dbm-BF₂ (**6**).

CAUTION! Although no problems were encountered in this work, transition metal perchlorate complexes with organic ligands are potentially explosive and should be handled with proper cautions.

Physical Measurements

C, H and N analyses were performed with a Perkin-Elmer 2400 series II analyzer at London Metropolitan University. Mass spectra were recorded using a matrix assisted laser desorption ionization with time of flight (MALDI-TOF) mass spectrometer ULTRAFLEXTREME (Bruker) at Servei de Proteòmica i Biologia Estructural (SePBioEs) from UAB. Infrared spectra (4000-450 cm⁻¹) were recorded from with a Perkin-Elmer Spectrum One Spectrometer. NMR spectra for ¹H, ¹³C and ¹⁹F were recorded in the different spectrometers at Servei de Resonància Magnètica Nuclear from Universitat Autònoma de Barcelona. UV-visible spectra for liquid samples were obtained on a Varian Cary 5000 using quartz cells. For solid samples a Diffuse Reflectance Sphere DRA-2500 accessory has been employed in a UV-Vis-NIR Varian Cary 5000 spectrophotometer, with operational range of 190-3300 nm, while measuring in reflectance or transmittance mode. Electrochemistry experiments were carried out in a Biologic SP-50 potentiostat controlled with EC-Lab V10.02 software. A standard three-electrode assembly (glassy carbon working together with auxiliary and reference platinum electrodes) was used with 0.1x10⁻³ M (NBu₄)(PF₆) as the supporting electrolyte. No IR compensation was employed. Quoted potentials are versus the ferrocene/ferrocenium couple, which was used as an internal standard. The scan rates for cyclic voltammetry (CV) and differential pulse voltammetry (DPV) were 50 and 50–100 mVs⁻¹, respectively. Distilled solvents were employed, and the concentrations of the compounds were approximately 10⁻³ M.

Conductance Measurements

In the mechanically-controlled break junction technique a controlled bending of a flexible substrate results in atomically sharp gold electrodes that can repeatedly be formed as the result of the breaking of a narrow gold constriction. Single molecules can bind to the uncoordinated Au atoms of the electrodes thereby forming molecular junctions. To improve the chances of these binding processes, molecules are terminated with appropriate anchoring groups. The conductance of **1-6** has been measured in air at room temperature. Details about the MCBJ setup and the measuring technique have been described elsewhere.^{4,5}

Computational Details

Molecular DFT calculations to perform full geometry optimizations using Gaussian09 code⁶ with the B3LYP hybrid exchange-correlation functional⁷ and a 6-311+G** basis set. In addition, MP2 calculations⁸ were also performed by using the same basis set. In the case of **3** (containing Cu^{II}), MP2 calculations were not performed due to the problem of such perturbative approach with open-shell systems. In the DFT calculations for the same compound, the dispersion contribution was included through the pair approach (D3) proposed by Grimme et al.⁹ Some single-point energy calculations were performed by employing the DLPNO-CCSD(T) (domain-based local pair natural orbital couple-cluster) method¹⁰ implemented in the Orca 4.0 code¹¹ with the def2-TZVPP basis set.¹² For such single-point calculations, the optimized structures at B3LYP and MP2 levels were used.

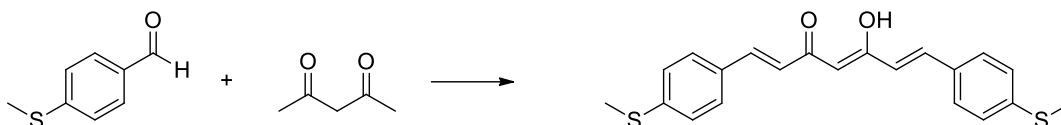
Geometry optimizations of the periodic systems with the two gold electrodes were carried out using the fhi-aims code¹³ using numerical basis set of “light” quality for the geometry optimization and a single-point energy of the optimized geometry with the “tight” basis set. The PBE functional¹⁴ was employed and a set of four k-points in the first Brillouin zone. A model unit cell was defined by a 2D 4x4 gold superlattice with a gold tip for the contact with the molecule (see Fig. S57). Full geometry optimization calculation (including cell parameters) was performed to analyze the stability of the conformers. In order to compare the total energies also the isolated molecules without the gold electrodes were optimized. Finally, full consistent non-equilibrium Green function (NEGF) calculations^{15,16} were performed using the ATK program (2016.3 version).¹⁷ The PBE exchange-correlation functional¹⁴ was employed combined with numerical wavefunction of double- ζ quality with polarization for all the atoms except the gold atoms using a single- ζ quality. A total number of 1664 k-points was using to calculate the properties (a symmetric grid of 8x8x52). The structure employed in the calculations is similar to the one presented in Fig. S57 with a 2D 4x4 gold superlattice including a tip of 10 gold atoms on each electrode (inset, Fig. 9). The distances between the anchoring S atoms to the Au atom from the tip of the electrodes was fixed to a value of 2.45 Å for all the molecules.

X-ray Diffraction

Single crystal diffraction data for all the compounds were collected on a Bruker APEXII SMART diffractometer at the Facultat de Química, Universitat de Barcelona, using a 30 microfocus Molybdenum $K\alpha$ radiation source. The structures were solved using direct methods or intrinsic phasing (SHELXS97, SHELXT-2014) and refined on F2 (SHELX-97). CCDC codes: 1833305 and 1840934. Hydrogen atoms were included on calculated positions, riding on their carrier atoms.

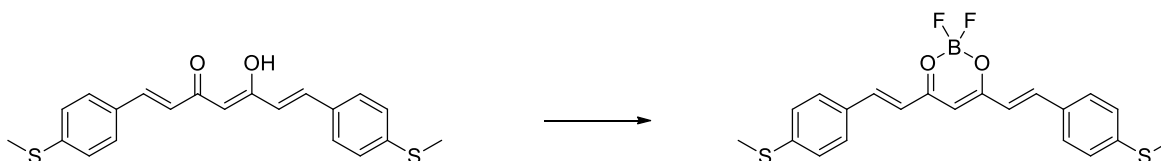
2. Synthetic procedures

Synthesis of compound 1.



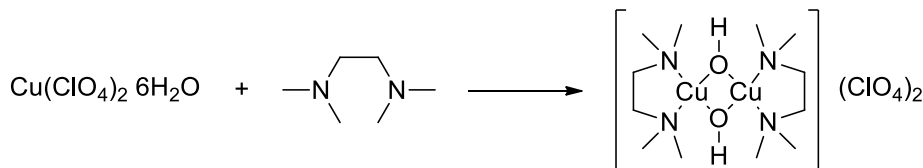
Synthesis of ((1E,4Z,6E)-5-hydroxy-1,7-bis(4-(methylthio)phenyl)hepta-1,4,6-triene-3-one), MeS-CCM (**1**): Acetylacetone (7 mmol, 0.72 mL) and B₂O₃ (5 mmol, 348.1 mg) were mixed in 10 mL of EtOAc and stirred at 50 °C for 30 min. After this, a white paste formed and tributylborate (14 mmol, 3.77 mL) was added and stirred for 15 min, subsequently, compound 4-(methylthio)benzaldehyde (14 mmol, 1.86 mL) was added and the reaction mixture was stirred at 50 °C for 3 h. Then, the reaction was cooled to room temperature for about 1 h, and a solution of *n*-butylamine (4 mmol, 0.4 mL) in 2 mL of EtOAc was added dropwise, and the reaction kept stirred at room temperature overnight. Overnight, the reaction turned to an orange-red colour with a colourful precipitate. This suspension was filtered and dried to afford a red solid which was suspended in 200 mL of H₂O stirred at room temperature for 8 h., filtered, washed with water and vacuum dried to afford 2.11 g of **1** as an orange precipitate. Yield: 82%. ¹H NMR (400 MHz, CDCl₃) δ 15.97 (s, 1H), 7.61 (d, *J* = 15.8 Hz, 2H), 7.47 (d, *J* = 8.4 Hz, 4H), 7.24 (d, *J* = 8.4 Hz, 4H), 6.58 (d, *J* = 15.8 Hz, 2H), 5.81 (s, 1H), 2.51 (s, 6H). ¹³C NMR (75 MHz, CDCl₃) δ 183.36, 141.91, 140.13, 131.73, 128.61, 126.21, 123.25, 101.91, 15.35. FTIR (KBr, ν / cm⁻¹): 3450, 3046, 1619, 1554, 1492, 1406, 1186, 1142, 1092, 973, 821, 502. Elemental analysis (%) calculated for C₂₁H₂₀O₂S₂: C 68.44, H 5.47; found C 68.28, H 5.41. MALDI-MS: *m/z* 368[M-H]⁻.

Synthesis of compound 2.

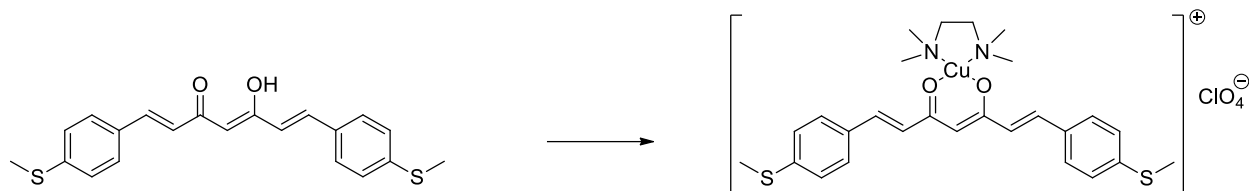


Synthesis of (2,2-difluoro-bis((E)-4-(methylthio)styryl)-1,3,2-dioxaborinane), MeS-CCM-BF₂ (**2**): In a 10 mL microwave vial, compound **1** (0.52 mmol, 191.6 mg) was dissolved in 5 mL of CH₂Cl₂. BF₃·Et₂O (0.62 mmol, 0.2 mL) was added to the solution and the reaction mixture was irradiated in a microwave reactor, reaching 60 °C during 5 min. After cooling, the dark purple suspension was filtered, washed with cold Et₂O and vacuum dried to afford 173 mg of **2** as a violet powder. Yield: 80%. ¹H-NMR (400 MHz, DMSO-d₆) δ 8.00 (d, *J* = 15.7 Hz, 2H), 7.81 (d, *J* = 8.4 Hz, 4H), 7.36 (d, *J* = 8.4 Hz, 4H), 7.18 (d, *J* = 15.7 Hz, 2H), 6.58 (s, 1H), 2.55 (s, 6H). ¹³C-NMR (101 MHz, DMSO-d₆) δ 179.43, 146.24, 144.45, 130.40, 130.00, 125.55, 120.12, 102.14, 14.01. ¹⁹F-NMR (188 MHz, DMSO-d₆) δ -137.58 (¹⁰B-F, 20%), -137.65 (¹¹B-F, 80%). FTIR (ν / cm⁻¹) 3024, 2928, 1603, 1589, 1505, 1491, 1408, 1293, 1164, 1058, 973, 958, 871, 818, 742, 596, 503, 419. Elemental analysis (%) calculated for C₂₁H₁₉BF₂O₂S₂: C 60.59, H 4.60; found C 60.48, H 4.60. MALDI-MS: *m/z* 415[M-H]⁻, 417[M+H]⁺.

Synthesis of compound 3.



Synthesis of Di- μ -hydroxo-bis(*N,N,N',N'*-tetramethylethylenediamine)dicooper(II) perchlorate, [CuOH(TMEDA)]₂(ClO₄)₂: Following experimental procedure from Meek *et al.*² Cu(ClO₄)₂·6H₂O (0.01 mol, 3.71 g) was dehydrated with 12 mL of 2,2-dimethoxypropane. The solution was filtered, diluted with 10 mL of absolute ethanol, and subsequently *N,N,N',N'*-tetramethylethylenediamine (0.01 mol, 2.90 mL) was added while stirring at room temperature. The resulting violet precipitate was recrystallized from dichloromethane. FTIR (KBr, ν / cm⁻¹) 3411, 2925, 1469, 1090, 1022, 953, 625, 482.



Synthesis of $[Cu^II(MeS-CCM)(TMEDA)]ClO_4$, MeS-CCM-Cu (**3**): The free ligand **1** (0.20 mmol, 74 mg) was dissolved in 10 mL of CH_2Cl_2 and stirred at ambient temperature. A solution of $[CuOH(TMEDA)]_2(ClO_4)_2$ (0.10 mmol, 59 mg) in CH_2Cl_2 (3 mL) was added dropwise to the ligand. Upon the addition, the reaction mixture changed from orange to brown. The reaction was kept stirring for 24 h. Afterward, an excess of Et_2O was added to precipitate the complex. The solid was re-dissolved in CH_2Cl_2 and layered with Et_2O to afford compound **5** as brown crystals. Yield: 74%. FTIR (KBr, ν / cm^{-1}) 3448, 2981, 2920, 1620, 1589, 1510, 1439, 1396, 1298, 1163, 1090, 987, 810, 623, 503, 445. Elemental analysis (%) calculated for $C_{27}H_{35}ClCuN_2O_6S_2$: C 50.14, H 5.46, N 4.33; found C 50.07, H 5.48, N 4.36. MALDI-MS: m/z 546[M]⁺.

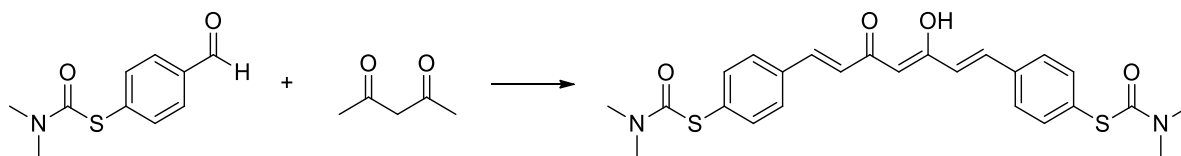
CAUTION! Although no problems were encountered in this work, transition metal perchlorate complexes with organic ligands are potentially explosive and should be handled with proper cautions.

Synthesis of compounds **4a** and **4**.

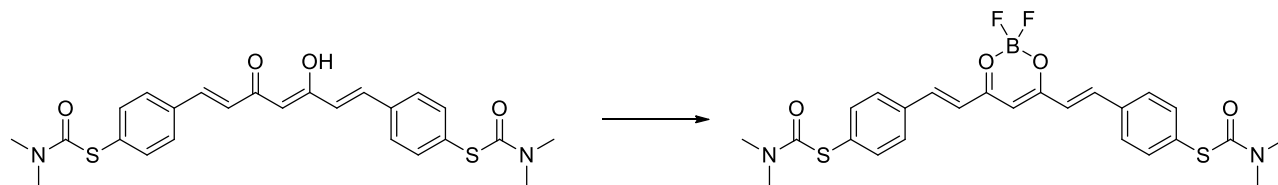


Synthesis of (*O*-4-formylphenyl) dimethylcarbamothioate: In a 100 mL round bottom flask, 4-hydroxybenzaldehyde (10 mmol, 1.22 g) and DABCO (20 mmol, 2.24 g) were dissolved in 20 mL of anhydrous DMF and stirred for 5 min at room temperature. Then, dimethylthiocarbamoyl chloride (20 mmol, 2.46 g) are added and the reaction mixture is kept at room temperature with stirring overnight. The reaction is quenched by pouring it over crushed ice (500 mL beaker full of ice), filtered, washed with water and vacuum dried to afford 1.96 g of the *O*-thiocarbamate as a white solid. Yield: 94 %. ¹H NMR (300 MHz, $CDCl_3$) δ 10.02 (s, 1H), 7.94 (d, $J = 8.7$ Hz, 2H), 7.26 (d, $J = 8.7$ Hz, 2H), 3.48 (s, 3H), 3.38 (s, 3H). ¹³C NMR (75 MHz, $CDCl_3$) δ 191.04, 186.85, 158.66, 134.17, 131.01, 123.84, 43.41, 39.00.

Synthesis of (*S*-4-formylphenyl) dimethylcarbamothioate: Using a modified method from Ge et al,¹ using a MW reactor. In a 10 mL microwave vial, the *O*-thiocarbamate (2.39 mmol, 500 mg) were dissolved in 5 mL of NMP and the reaction was irradiated in the microwave reactor reaching a temperature of 220 °C for 40 min. Then, the reaction was cooled to room temperature by a flow of compressed air. The reaction is quenched by pouring it over crushed ice (100 mL beaker full of ice), filtered and vacuum dried to afford 277 mg of the *S*-carbamate as a brownish solid. Yield: 55 %. ¹H NMR (300 MHz, $CDCl_3$) δ 10.02 (s, 1H), 7.87 (d, $J = 8.3$ Hz, 2H), 7.67 (d, $J = 8.3$ Hz, 2H), 3.07 (s, 6H). ¹³C NMR (75 MHz, $CDCl_3$) δ 191.67, 165.45, 136.89, 136.39, 135.68, 129.82, 37.12.



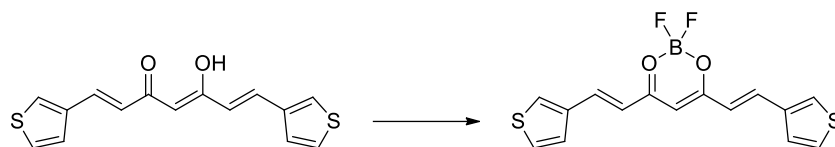
Synthesis of (*S,S'*-(((1*E*,4*Z*,6*E*)-3-hydroxy-5-oxohepta-1,3,6-triene-1,7-diyl)bis(4,1-phenylene)) bis(dimethyl-carbamothioate)), S-CCM (**4a**): The synthetic procedure and workout are identical to that described for **1** but using *S*-carbamatebenzaldehyde (5 mmol, 1.05 g) instead. 237 mg of **4** were obtained as a light yellow precipitate. Yield: 20%. ¹H NMR (300 MHz, $CDCl_3$) δ 15.81 (s, 1H), 7.65 (d, $J = 15.9$ Hz, 2H), 7.55 (d, $J = 8.5$ Hz, 4H), 7.51 (d, $J = 8.5$ Hz, 4H), 6.64 (d, $J = 15.9$ Hz, 2H), 5.86 (s, 1H), 3.06 (s, 12H). ¹³C NMR (75 MHz, $CDCl_3$) δ 183.24, 166.37, 139.90, 135.98, 135.11, 131.18, 128.47, 125.22, 102.25, 37.07. FTIR (ν / cm^{-1}) 2924, 1650, 1630, 1480, 1402, 1358, 1254, 1085, 1014, 968, 906, 822, 684. Elemental analysis (%) calculated for $C_{21}H_{19}N_2O_4S_2 \cdot 1.2CO_2 \cdot 2H_2O$: C 55.07, H 5.29, N 4.90; found C 54.87, H 5.50, N 4.87. MALDI-MS: m/z 481[M-H]⁻.



Synthesis of (2,2-difluoro-bis(*S*-(*E*)-4-(dimethyl-carbamothioate)styryl))-1,3,2-dioxaborinane, S-CCM-BF₂ (**4**): Compound **4** was achieved as a red powder by following the procedure described in **2**, but using S-CCM (**4a**). Yield: 84%. ¹H NMR (400 MHz, CD₂Cl₂-d₂) δ 8.06 (d, *J* = 15.7 Hz, 2H), 7.66 (d, *J* = 8.2 Hz, 4H), 7.57 (d, *J* = 8.2 Hz, 4H), 6.85 (d, *J* = 15.7 Hz, 2H), 6.22 (s, 1H), 3.07 (s, 6H), 3.02 (s, 6H). ¹⁹F NMR (376 MHz, CD₂Cl₂-d₂) δ -140.19 (¹⁰B-F, 20%), -140.25 (¹¹B-F, 80%). FTIR (ν / cm⁻¹) 2933, 1664, 1614, 1516, 1402, 1360, 1301, 1164, 1085, 1056, 1003, 974, 828, 682. Elemental analysis (%) calculated for C₂₅H₂₅BF₂N₂O₄S₂·1.1CO₂·2H₂O: C 50.99, H 4.75, N 4.56; found C 50.66, H 4.37, N 4.93. MALDI-MS: m/z 529[M-H]⁻, 553[M+Na]⁺.

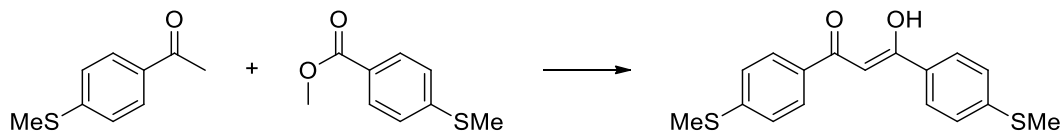
Synthesis of compounds 5a and 5.

Synthesis of ((*1E,4Z,6E*)-5-hydroxy-1,7-di(thiophen-3-yl)hepta-1,4,6-trien-3-one), Thph-CCM (**5a**): Following experimental procedure from Etcheverry-Berríos et al.³ Acetylacetone (7 mmol, 0.72 mL) and B₂O₃ (5 mmol, 348.1 mg) were suspended in 10 mL of EtOAc and stirred at 50 °C for 30 min. After this, a white paste formed and tributylborate (14 mmol, 3.77 mL) was added and stirred for 15 min, subsequently, compound thiophen-3-carboxaldehyde (14 mmol, 1.22 mL) was added and the reaction mixture was stirred at 50 °C for 3 h. Then, the reaction was cooled to room temperature for about 1 h, and a solution of *n*-butylamine (4 mmol, 0.4 mL) in 2 mL of EtOAc was added dropwise, and the reaction kept stirred at room temperature overnight. The next day, the reaction turned to an orange colour with precipitate. This suspension was filtered and dried to afford an orange solid which was suspended in 200 mL of H₂O stirred at room temperature for 8 h., filtered, washed with water and vacuum dried. The yellow precipitate was recrystallized from hot MeCN to afford 732 mg of the product as yellow needle-like crystals. Yield: 36 %. ¹H NMR (300 MHz, CDCl₃) δ 15.81 (s, 1H), 7.65 (d, *J* = 15.9 Hz, 2H), 7.55 (d, *J* = 8.5 Hz, 4H), 7.51 (d, *J* = 8.5 Hz, 4H), 6.64 (d, *J* = 15.9 Hz, 2H), 5.86 (s, 1H), 3.06 (s, 12H). ¹³C NMR (75 MHz, CDCl₃) δ 183.24, 166.37, 139.90, 135.98, 131.18, 128.47, 125.22, 102.25, 37.07.

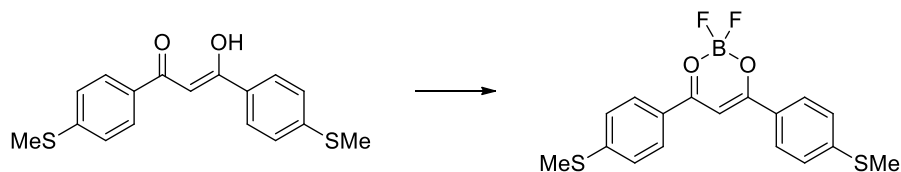


Synthesis of (2,2-difluoro-bis(*E*)-2-(thiophen-3-yl)vinyl)-1,3,2-dioxaborinane, Thph-CCM-BF₂ (**5**): Compound **5** was achieved as an orange powder following the same procedure described for **2**, but using Thph-CCM (**5a**). Yield: 85 %. ¹H-NMR (400 MHz, CDCl₃) δ 8.05 (d, *J* = 15.4 Hz, 2H), 7.71 (d, *J* = 1.8 Hz, 2H), 7.43-7.34 (m, 4H), 6.53 (d, *J* = 15.5 Hz, 2H), 6.04 (s, 1H). ¹³C-NMR (50 MHz, DMSO-*d*₆) δ 179.91, 140.38, 137.91, 133.68, 128.50, 120.73, 101.69. ¹⁹F-NMR (376 MHz, DMSO-*d*₆) δ -140.63 (¹⁰B-F, 20 %), -140.69 (¹¹B-F, 80 %). FTIR (ν / cm⁻¹) 3442, 1603, 1547, 1495, 1412, 1390, 1149, 974, 744. Elemental analysis (%) calculated for C₁₅H₁₁BF₂O₂S₂: C 53.59, H 3.30; found C 53.67, H 3.17. MALDI-MS: m/z 334[M-H]⁻, 316[M-F]⁺.

Synthesis of compounds 6a and 6.



Synthesis of (*Z*)-3-hydroxy-1,3-bis(4-(methylthio)phenyl)prop-2-en-1-one, MeS-dbm (**6a**): Methyl 4-(methylthio)benzoate (1.82 g, 10 mmol) and NaH (0.53 g) were suspended in 30 mL of anhydrous THF, and stirred at room temperature. Separately, 4-(methylthio)acetophenone (1.66 g, 10 mmol) was dissolved in 20 mL of anhydrous THF. This solution was added dropwise to the NaH/methyl 4-(methylthio)benzoate suspension with stirring and gently heating the mixture to 70 °C. After a couple of minutes the reaction turned into a dark red colour. The reaction is kept under stirring, refluxing at 70 °C for 24 h. Then, the reaction is cooled to room temperature and 30 mL of H₂O are added. After stirring for 15 minutes, the pH of the reaction was adjusted to 7 using conc. HCl, turning the red solution into an orange two-phase system, then, more water is added until the appearance of an orange precipitate. The reaction is then put in a water-ice bath and stirred for 15 minutes more. Then the reaction is filtered, washed with cold EtOH, and vacuum dried to afford 1.75 g of a bright yellow crystalline. Yield: 55 %. ¹H-NMR (300 MHz, CDCl₃) δ 16.98 (s, 1H), 7.89 (d, *J* = 8.6 Hz, 4H), 7.30 (d, *J* = 8.6 Hz, 4H), 6.77 (s, 1H), 2.53 (s, 6H). ¹³C-NMR (75 MHz, CDCl₃) δ 184.91, 145.12, 131.97, 127.61, 125.51, 92.33, 77.16, 15.07. FTIR (KBr, ν / cm⁻¹): 1574, 1508, 1419, 1295, 1188, 1010, 956, 830, 768. Elemental analysis (%) calculated for C₁₇H₁₆O₂S₂·0.9H₂O: C 61.38, H 5.39; found C 61.41, H 5.40. MALDI-MS: m/z 317[M+H]⁺, 339[M+Na]⁺.



Synthesis of 2,2-difluoro-bis(4-(methylthio)phenyl)-1,3,2-dioxaborinane, MeS-dbm-BF₂ (6): In a 10 mL microwave vial, compound **6a** (0.96 mmol, 304 mg) was suspended in 2 mL of CH₂Cl₂. To this, BF₃·Et₂O (1.15 mmol, 0.14 mL) were added and the reaction mixture was irradiated in a microwave reactor, reaching 60 °C and maintained at this temperature for 5 min. After cooling with a flow of compressed air, the red suspension is filtered, washed with cold Et₂O and vacuum dried to afford 297 mg of **6** as an orange powder. Yield: 85 %. ¹H-NMR (300 MHz, CDCl₃) δ 8.03 (d, *J* = 8.7 Hz, 4H), 7.33 (d, *J* = 8.7 Hz, 4H), 7.07 (s, 1H), 2.57 (s, 6H). ¹³C NMR (101 MHz, CDCl₃) δ 181.47, 149.75, 129.20, 128.05, 125.31, 92.38, 14.78. ¹⁹F-NMR (235 MHz, CDCl₃) δ -140.86 (¹⁰B-F, 20 %), -140.92 (¹¹B-F, 80 %). FTIR (ν / cm⁻¹) 1588, 1537, 1478, 1412, 1364, 1249, 1106, 1027, 816, 794. Elemental analysis (%) calculated for C₁₇H₁₅BF₂O₂S₂: C 56.06, H 4.15; found C 55.93, H 4.01. MALDI-MS: *m/z* 345[M-F]⁺, 387[M+Na]⁺.

3. Crystallographic data of **1**

Ligand MeS-CCM (**1**) crystallizes in the orthorhombic space group $P2_1/n$ with the asymmetric unit described as one molecule of the ligand. A POV-Ray representation of the labeled molecule is presented below. The ligand is composed of a 1,4,6-heptatriene chain containing a β -diketone moiety at the center of the chain (C2, C1 and C12), in the enol tautomer and the terminal carbons (C4 and C14) are bound to two *p*-methylthiophenyl groups by the carbon on the position 4 (C5 and C15). A β -diketone group, typically shows an equilibrium between two tautomeric forms with rapidly interconversion. Analyzing the bond distances of compound **1**, the crystal structure shows the stabilization of the enol tautomer. The crystal structure shows a non-planar structure where the chain is bended towards the center of the molecule.

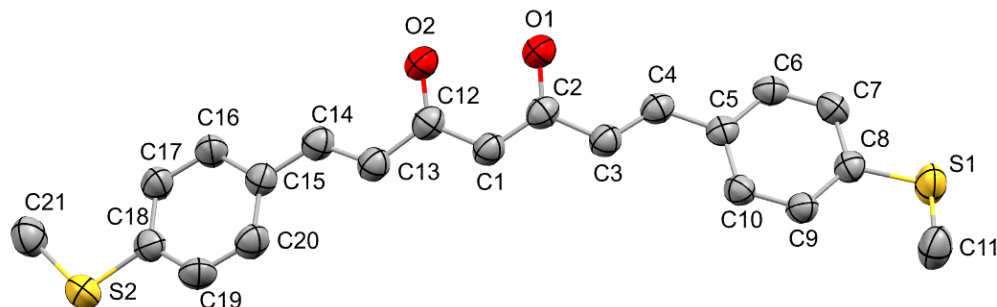


Figure S1. View of **1** with thermal ellipsoids fixed at 50 %. H atoms are omitted for the sake of simplification. Color legend: O in red, C in gray and sulfur in yellow.

Table S1. General crystallographic data for **3**.

	Compound 1
Chemical formula	$C_{21}H_{20}O_2S_2$
MW / $g \cdot mol^{-1}$	368.51
Space group	$P2_1/n$
$a / \text{\AA}$	13.7982(5)
$b / \text{\AA}$	5.5253(2)
$c / \text{\AA}$	24.9052(8)
$\alpha / ^\circ$	90
$\beta / ^\circ$	103.390(2)
$\gamma / ^\circ$	90
$V / \text{\AA}^3$	1847.14
Z	2
R	0.0432

Table S2. Selected bond distances for **1**.

S2	C18	1.756(2)	C10	C9	1.377(3)
S2	C21	1.779(3)	C6	C7	1.372(3)
S1	C8	1.756(2)	C12	C13	1.451(3)
S1	C11	1.775(3)	C12	C1	1.407(3)
O2	C12	1.280(3)	C14	C13	1.327(3)
O1	C2	1.301(3)	C8	C7	1.383(3)
C5	C4	1.456(3)	C8	C9	1.394(3)
C5	C10	1.392(3)	C2	C3	1.452(3)
C5	C6	1.395(3)	C2	C1	1.384(3)
C4	C3	1.330(3)	C18	C17	1.374(3)
C15	C14	1.449(3)	C18	C19	1.397(3)
C15	C20	1.390(3)	C20	C19	1.367(3)
C15	C16	1.392(3)	C17	C16	1.379(3)

Table S3. Selected bond angles for **1**.

C18	S2	C21	103.6(1)	S1	C8	C9	123.9(2)
C8	S1	C11	104.3(1)	C7	C8	C9	118.7(2)
C4	C5	C10	123.3(2)	C12	C13	C14	122.3(2)
C4	C5	C6	119.2(2)	O1	C2	C3	117.4(2)
C10	C5	C6	117.5(2)	O1	C2	C1	121.0(2)
C5	C4	C3	127.7(2)	C3	C2	C1	121.6(2)
C14	C15	C20	123.8(2)	C6	C7	C8	120.8(2)
C14	C15	C16	119.5(2)	C10	C9	C8	120.2(2)
C20	C15	C16	116.7(2)	C4	C3	C2	122.8(2)
C5	C10	C9	121.5(2)	S2	C18	C17	124.3(2)
C5	C6	C7	121.3(2)	S2	C18	C19	117.4(2)
O2	C12	C13	119.5(2)	C17	C18	C19	118.3(2)
O2	C12	C1	120.3(2)	C12	C1	C2	121.5(2)
C13	C12	C1	120.1(2)	C15	C20	C19	121.3(2)
C15	C14	C13	128.5(2)	C18	C17	C16	120.0(2)
S1	C8	C7	117.4(2)				

4. Crystallographic data of **3**

Complex MeS-Cu-CCM (**3**) crystallizes in the monoclinic space group $P2_1/c$ with the asymmetric unit described as $[\text{Cu}(\text{MeS-CCM})(\text{TMEDA})]\text{ClO}_4 \cdot 2\text{CH}_2\text{Cl}_2$. A POV-Ray representation of the labeled molecule is presented below. Each molecule contains a pentacoordinated Cu^{II} site with a square pyramidal geometry, each site bonded to one MeS-CCM ligand through the β -diketone moiety, one TMEDA molecule linked through the nitrogen atoms, and a perchlorate anion in the apical position. The Cu-O(1) and Cu-O(2) bond distances are 1.901 Å and 1.911 Å, respectively, whereas the Cu-N distances are 2.060 Å and 2.014 Å for Cu-N(1) and Cu-N(2). Finally, the distance between the Cu site and the perchlorate anion (Cu-O(6)) is 2.625 Å. The bond angles around the Cu^{II} ion are in agreement with previously observed five-coordinated square-pyramidal copper complexes, being the O-Cu-O angle of 93.99° and the N-Cu-N angle of 86.20° . In the crystal, the phenyl rings of the curcuminoid ligand overlaps in a face-to-face manner through π - π stacking, with interplanar distances in the range of 3.71 – 3.75 Å.

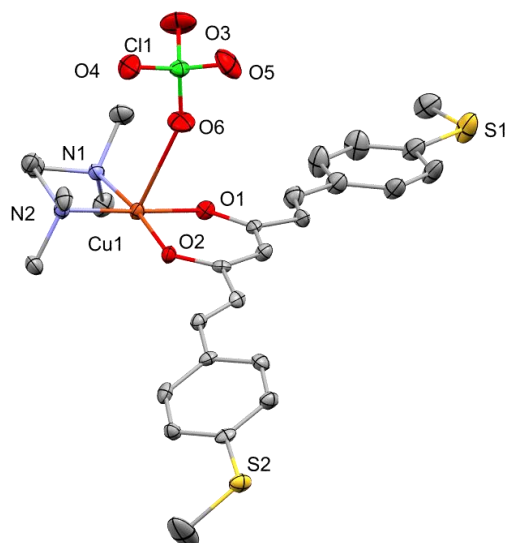


Figure S2. View of **3** with thermal ellipsoids fixed at 50 %. Two CH_2Cl_2 molecules and H atoms are omitted for the sake of simplification. Color legend: Cu in orange, O in red, N in blue, C in gray and sulfur in yellow.

Table S4. General crystallographic data for **3**.

	Compound 3
Chemical formula	$\text{C}_{27}\text{H}_{39}\text{ClCuN}_2\text{O}_6\text{S}_2 \cdot 2\text{CH}_2\text{Cl}_2$
MW / $\text{g}\cdot\text{mol}^{-1}$	816.57
Space group	$P2_1/c$
$a / \text{Å}$	8.4746(7)
$b / \text{Å}$	9.5148(7)
$c / \text{Å}$	45.506(3)
$\alpha / ^\circ$	90
$\beta / ^\circ$	91.765(4)
$\gamma / ^\circ$	90
$V / \text{Å}^3$	3667.6
Z	4
R	0.0688

Table S5. Selected bond distances for **3**.

Cu1	O1	1.901(3)	S2	C24	1.759(5)
Cu1	O2	1.911(3)	S2	C27	1.783(8)
Cu1	N1	2.060(4)	N1	C1	1.473(7)
Cu1	N2	2.014(4)	N1	C2	1.494(7)
Cu1	O6	2.625(4)	N1	C3	1.492(7)
O1	C8	1.286(6)	N2	C4	1.495(7)
O2	C18	1.282(5)	N2	C5	1.476(7)
S1	C14	1.762(6)	N2	C6	1.486(7)
S1	C17	1.773(7)			

Table S6. Selected bond angles for **3**.

O1	Cu1	O2	94.0(1)	Cu1	O1	C8	125.5(3)
O1	Cu1	N1	89.2(2)	Cu1	O2	C18	125.3(3)
O1	Cu1	N2	175.3(2)	Cu1	N1	C1	111.0(3)
O1	Cu1	O6	83.5(1)	Cu1	N1	C2	108.6(3)
O2	Cu1	N1	173.3(2)	Cu1	N1	C3	107.7(3)
O2	Cu1	N2	90.6(2)	C2	N1	C3	110.3(4)
O2	Cu1	O6	86.9(1)	Cu1	N2	C4	104.3(3)
N1	Cu1	N2	86.2(2)	Cu1	N2	C5	115.5(3)
N1	Cu1	O6	99.4(1)	Cu1	N2	C6	107.4(3)
N2	Cu1	O6	97.7(1)				

5. ^1H , ^{13}C , ^{19}F NMR spectra of Curcuminoids

^1H NMR (400 MHz, CDCl_3) δ 15.97 (s, 1H), 7.61 (d, $J = 15.8$ Hz, 2H), 7.47 (d, $J = 8.4$ Hz, 4H), 7.24 (d, $J = 8.4$ Hz, 4H), 6.58 (d, $J = 15.8$ Hz, 2H), 5.81 (s, 1H), 2.51 (s, 6H).

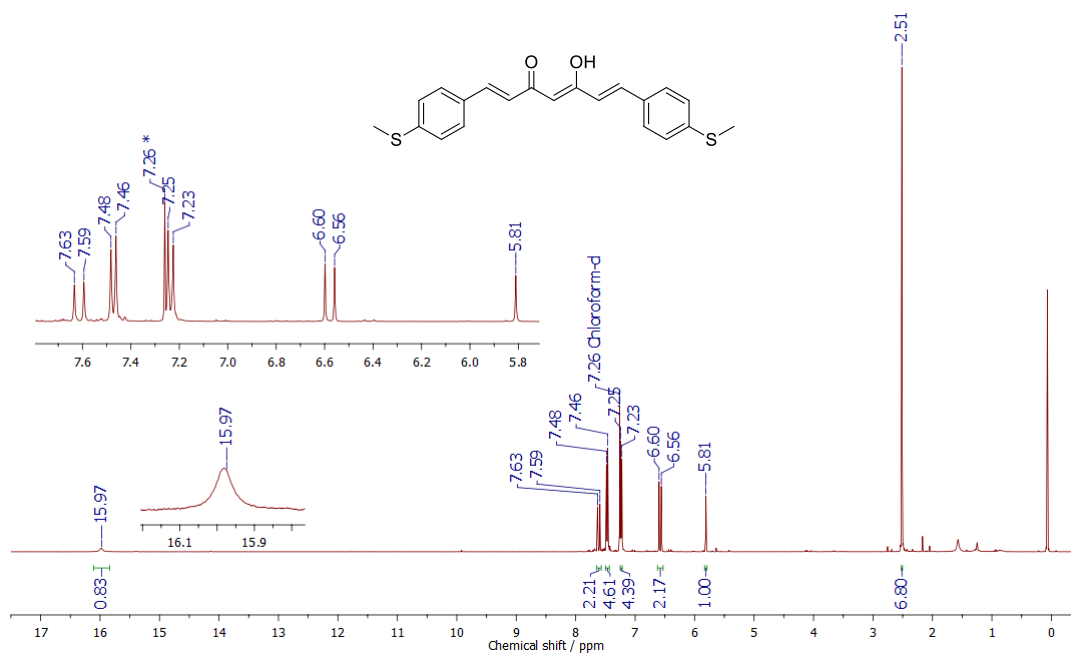


Figure S3. ^1H NMR spectrum of **1** in CDCl_3 at 292 K.

^{13}C NMR (101 MHz, CDCl_3) δ 183.36, 141.91, 140.13, 131.73, 128.61, 126.21, 123.25, 101.91, 15.35.

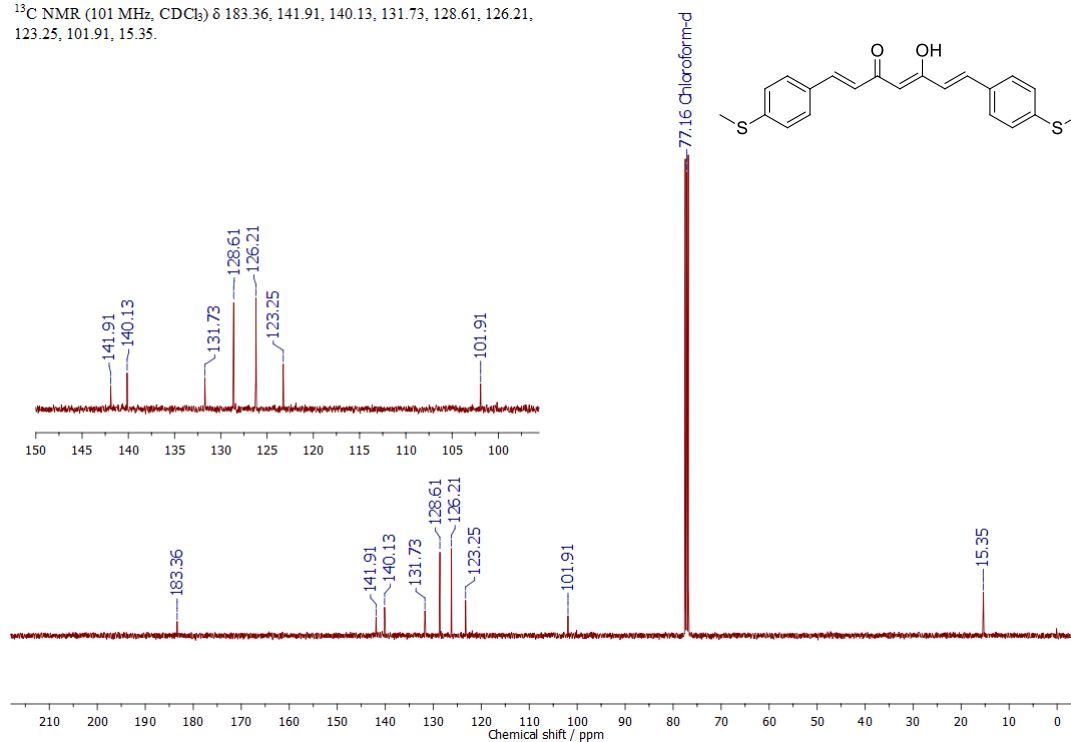


Figure S4. ^{13}C NMR spectrum of **1** in CDCl_3 at 300 K.

^1H NMR (400 MHz, CD_2Cl_2) δ 8.00 (d, $J = 15.6$ Hz, 2H), 7.58 (d, $J = 8.4$ Hz, 4H), 7.29 (d, $J = 8.4$ Hz, 4H), 6.75 (d, $J = 15.6$ Hz, 2H), 6.12 (s, 1H), 2.54 (s, 6H).

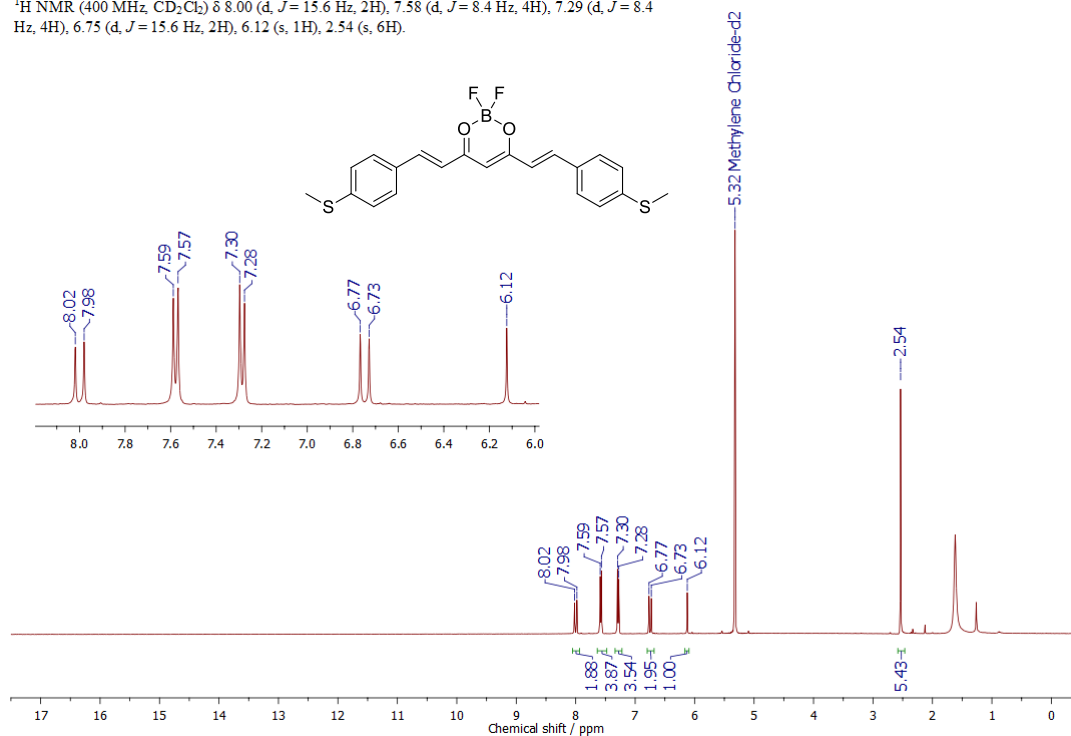


Figure S5. ^1H NMR spectrum of **2** in CD_2Cl_2 at 292 K.

^{13}C NMR (101 MHz, DMSO) δ 179.43, 146.24, 144.45, 130.40, 130.00, 125.55, 120.12, 102.14, 14.00.

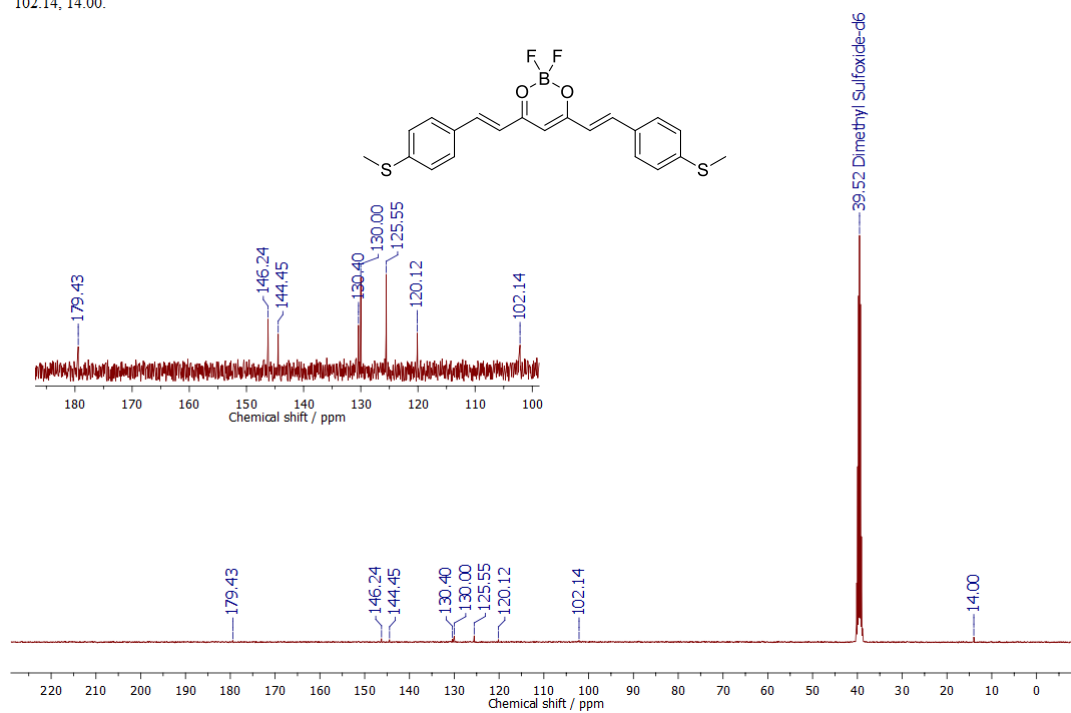


Figure S6. ^{13}C NMR spectrum of **2** in DMSO-d_6 at 297 K.

^{19}F NMR (188 MHz, DMSO) δ -137.58, -137.65.

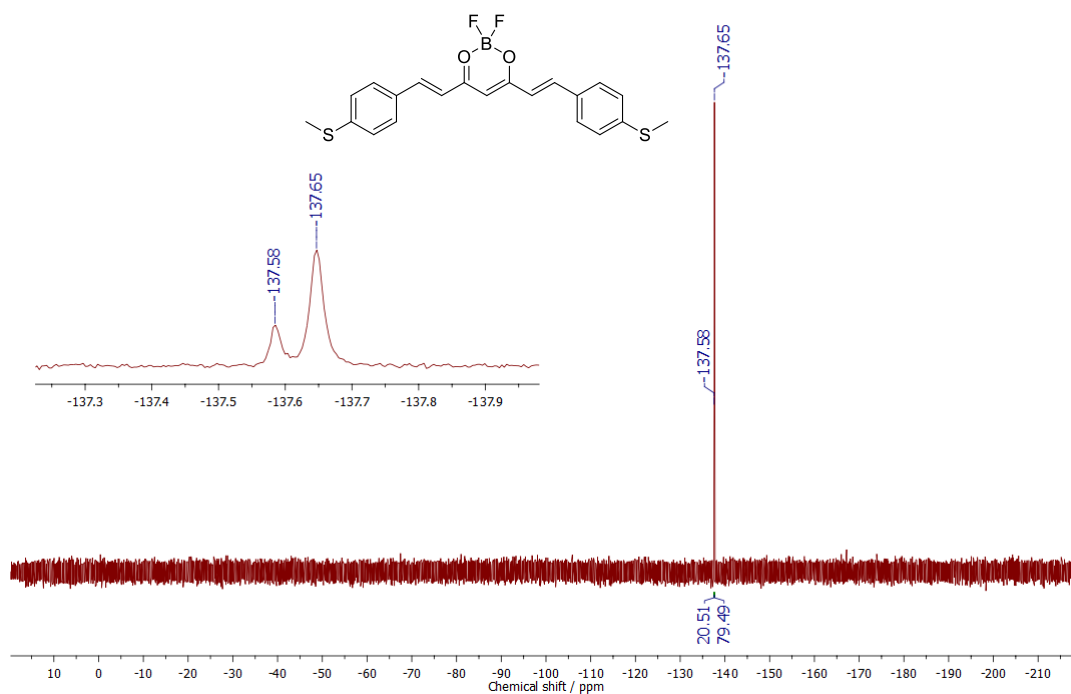


Figure S7. ^{19}F NMR spectrum of **2** in DMSO- d_6 at 300 K.

^1H NMR (300 MHz, CDCl_3) δ 15.81 (s, 1H), 7.65 (d, $J = 15.9$ Hz, 2H), 7.55 (d, $J = 8.5$ Hz, 4H), 7.51 (d, $J = 8.5$ Hz, 4H), 6.64 (d, $J = 15.9$ Hz, 2H), 5.86 (s, 1H), 3.06 (s, 12H).

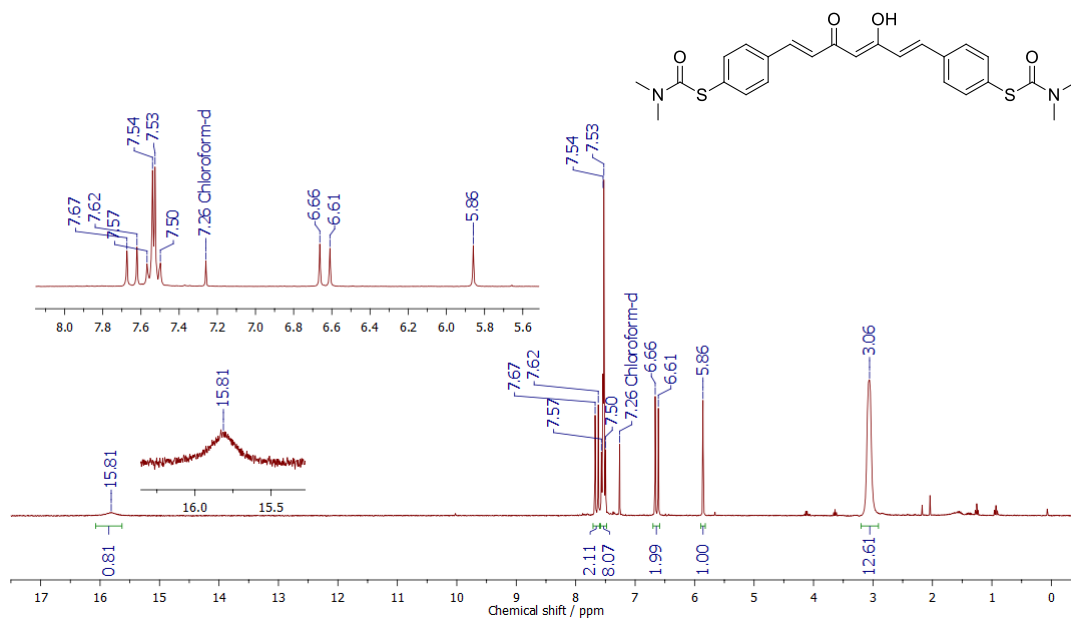


Figure S8. ^1H NMR spectrum of **4a** in CDCl_3 at 293 K.

^{13}C NMR (75 MHz, CDCl_3) δ 183.23, 166.37, 139.90, 135.98, 135.80, 131.18, 128.46, 125.22, 102.25, 37.07.

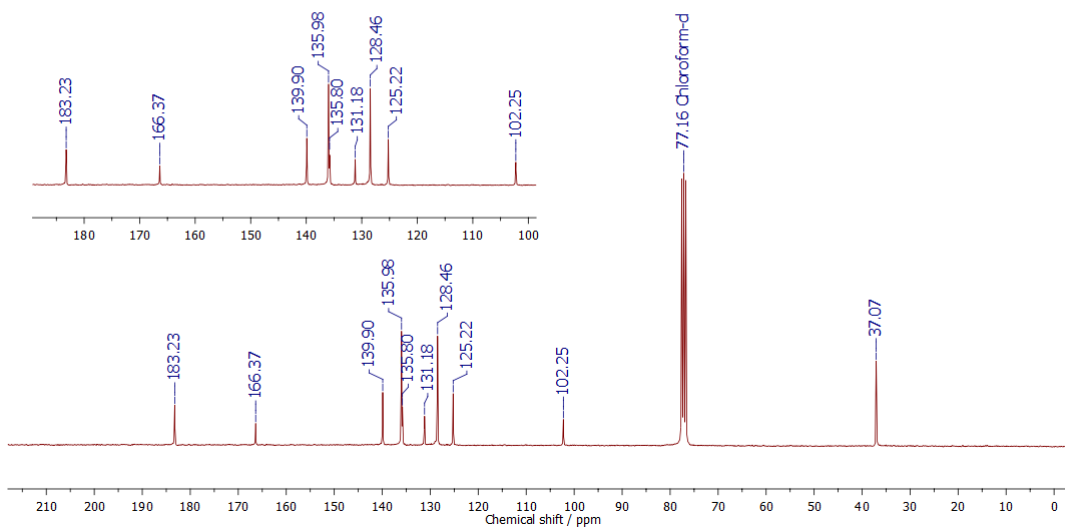
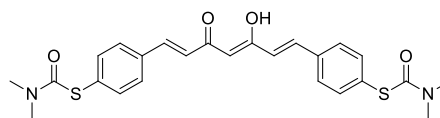


Figure S9. ^{13}C NMR spectrum of **4a** in CDCl_3 at 293 K.

^1H NMR (400 MHz, CD_2Cl_2) δ 8.06 (d, $J = 15.7$ Hz, 2H), 7.66 (d, $J = 8.3$ Hz, 4H), 7.57 (d, $J = 8.3$ Hz, 4H), 6.85 (d, $J = 15.7$ Hz, 2H), 6.22 (s, 1H), 3.07 (s, 6H), 3.02 (s, 6H).

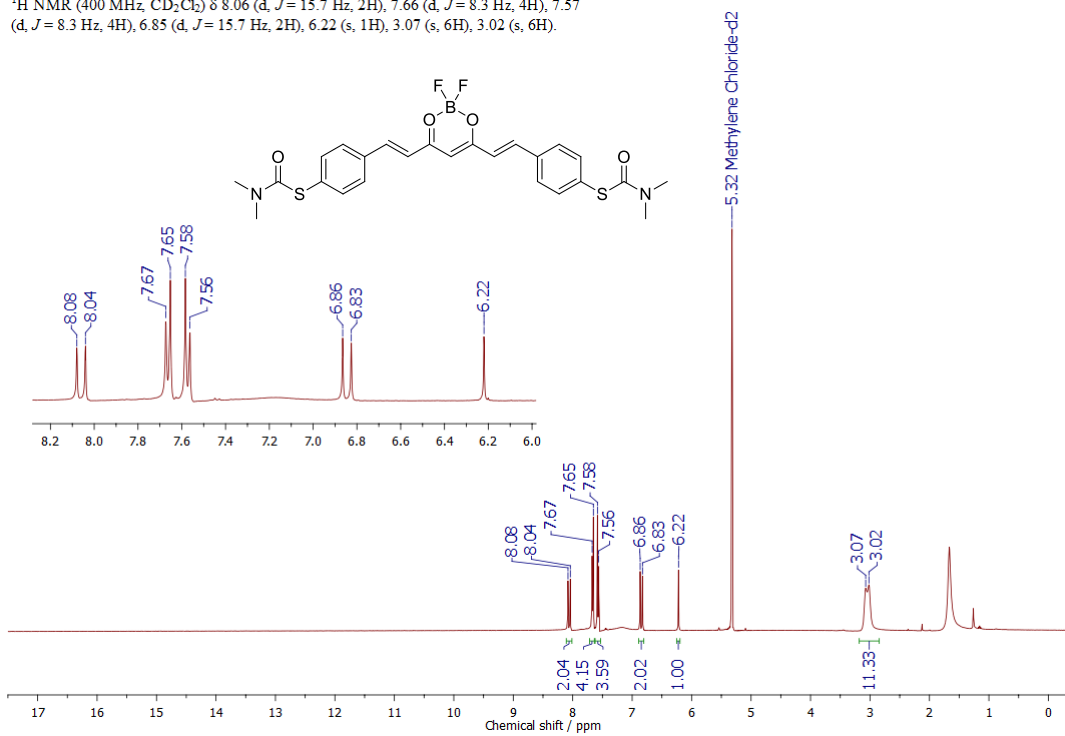


Figure S10. ^1H NMR spectrum of **4** in CD_2Cl_2 at 298 K.

^{19}F NMR (376 MHz, CD_2Cl_2) δ -140.19, -140.25.

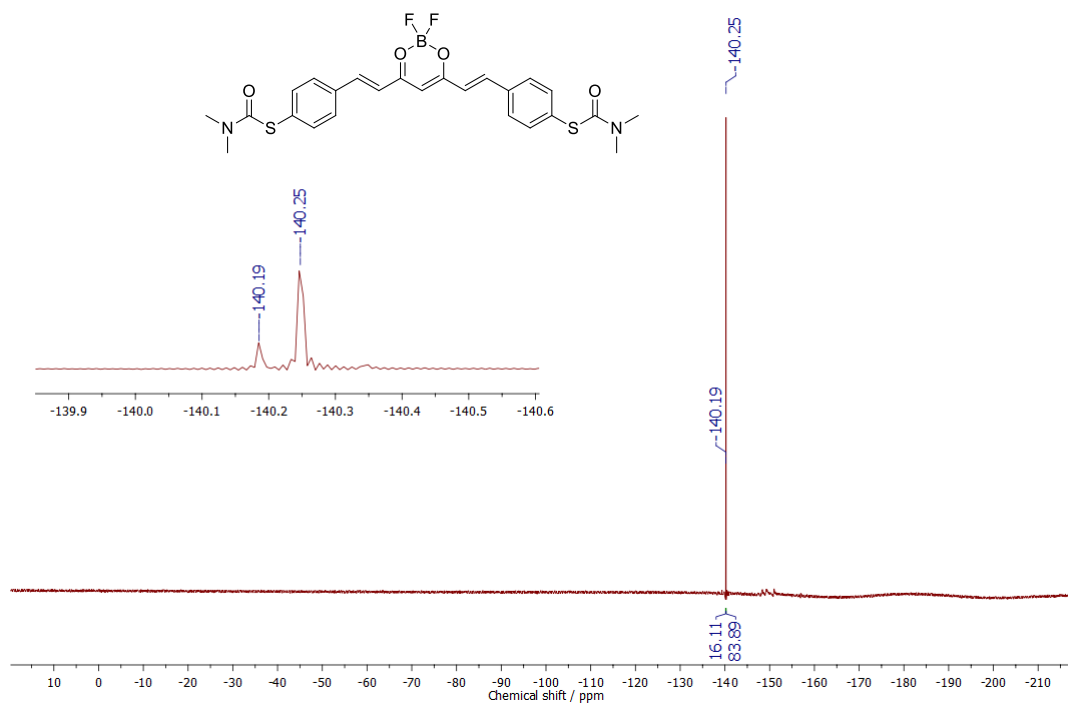


Figure S11. ^{19}F NMR spectrum of **4** in CD_2Cl_2 at 298 K.

^1H NMR (400 MHz, DMSO) δ 8.26 (d, $J = 2.2$ Hz, 2H), 8.05 (d, $J = 15.7$ Hz, 2H), 7.71 (dd, $J = 4.9, 2.2$ Hz, 2H), 7.66 (d, $J = 4.9$ Hz, 2H), 7.02 (d, $J = 15.6$ Hz, 2H), 6.53 (s, 1H).

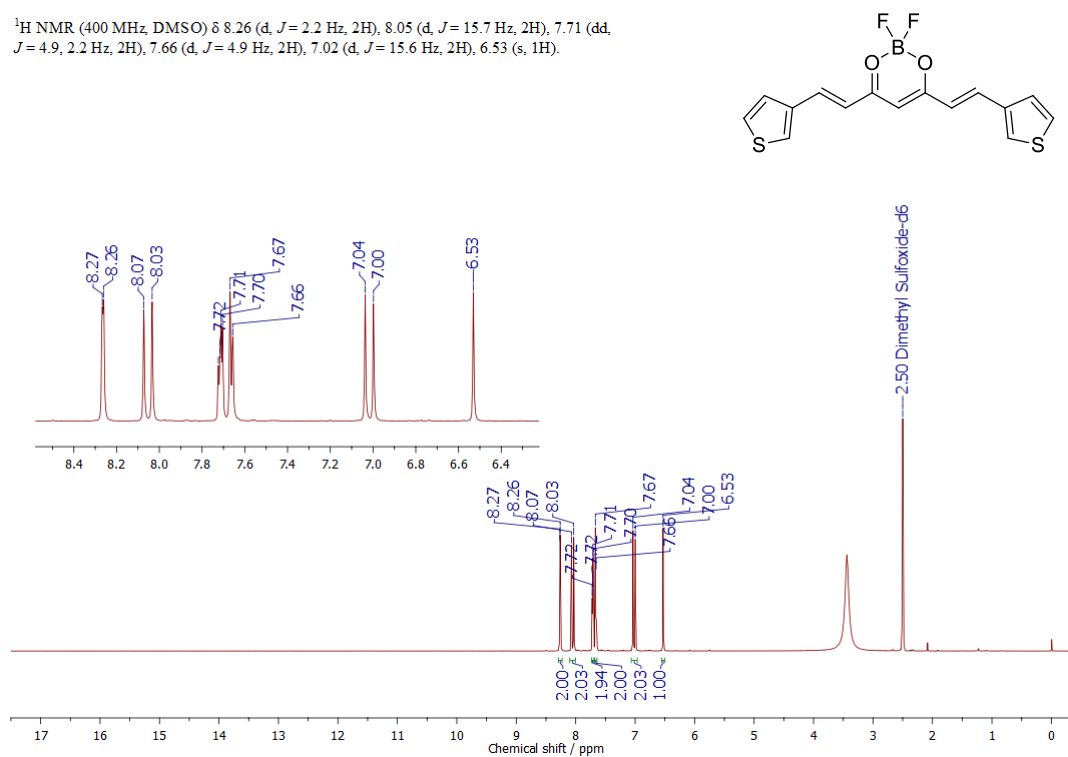


Figure S12. ^1H NMR spectrum of **5** in DMSO- d_6 at 300 K.

^{13}C NMR (50 MHz, DMSO) δ 179.91, 140.38, 137.91, 133.68, 128.50, 125.89, 120.73, 101.69.

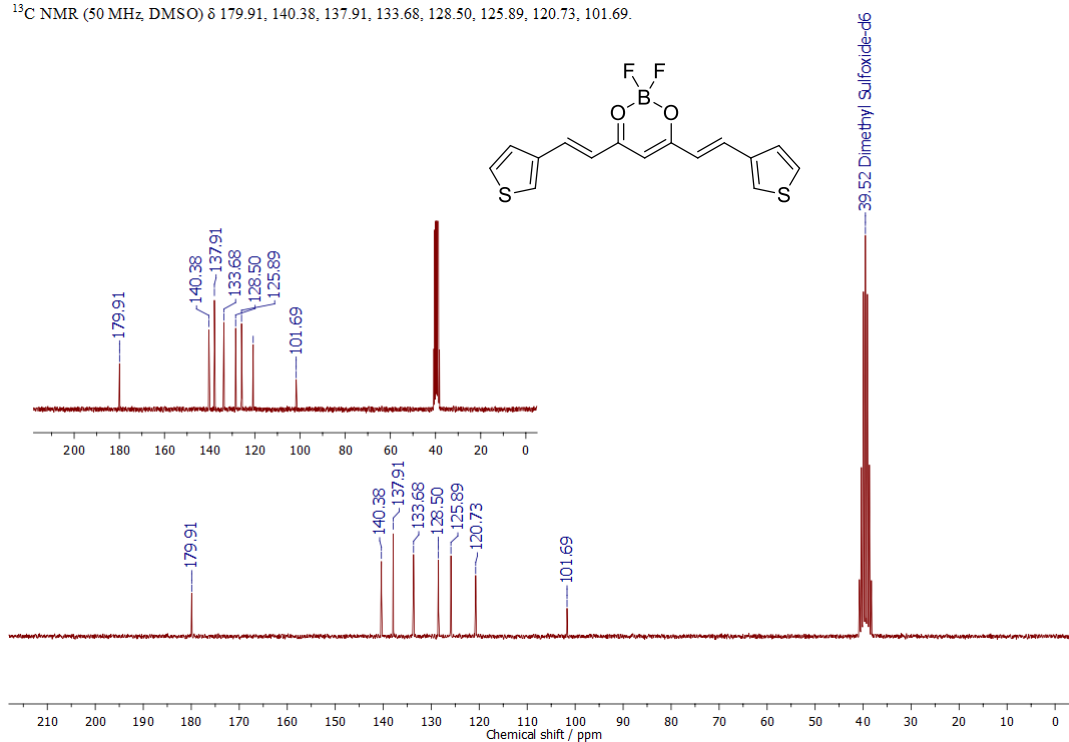


Figure S13. ^{13}C NMR spectrum of **5** in DMSO- d_6 at 300 K.

^{19}F NMR (376 MHz, CDCl_3) δ -140.63, -140.69.

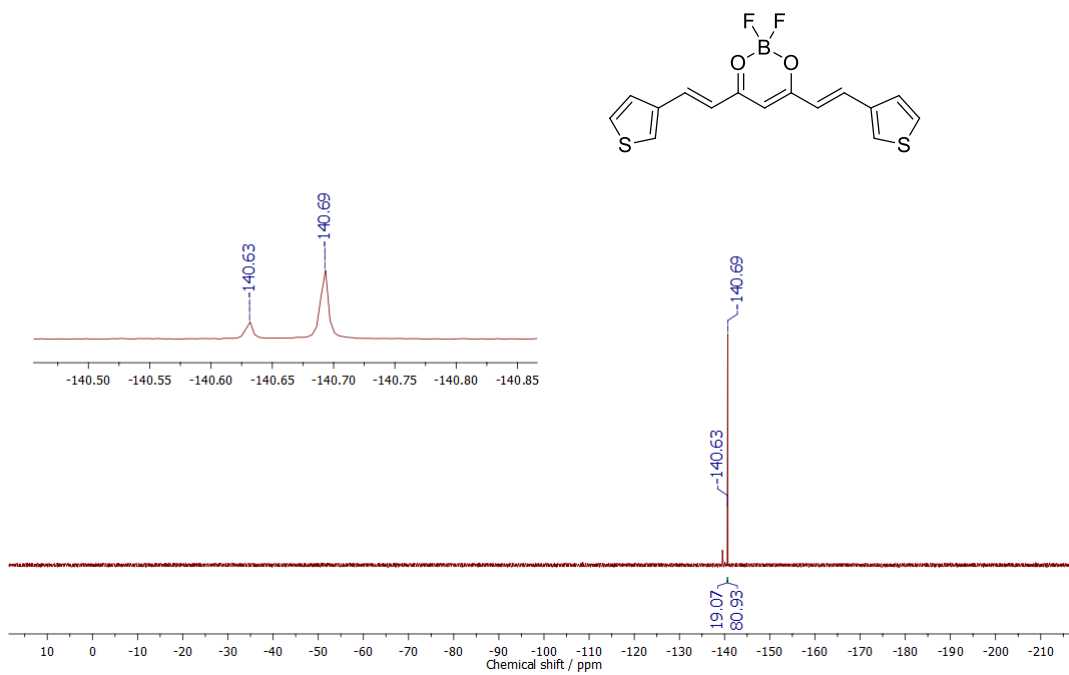


Figure S14. ^{19}F NMR spectrum of **5** in DMSO- d_6 at 300 K.

^1H NMR (300 MHz, CDCl_3) δ 16.98 (s, 1H), 7.89 (d, $J = 8.6$ Hz, 4H), 7.30 (d, $J = 8.6$ Hz, 4H), 6.77 (s, 1H), 2.53 (s, 6H).

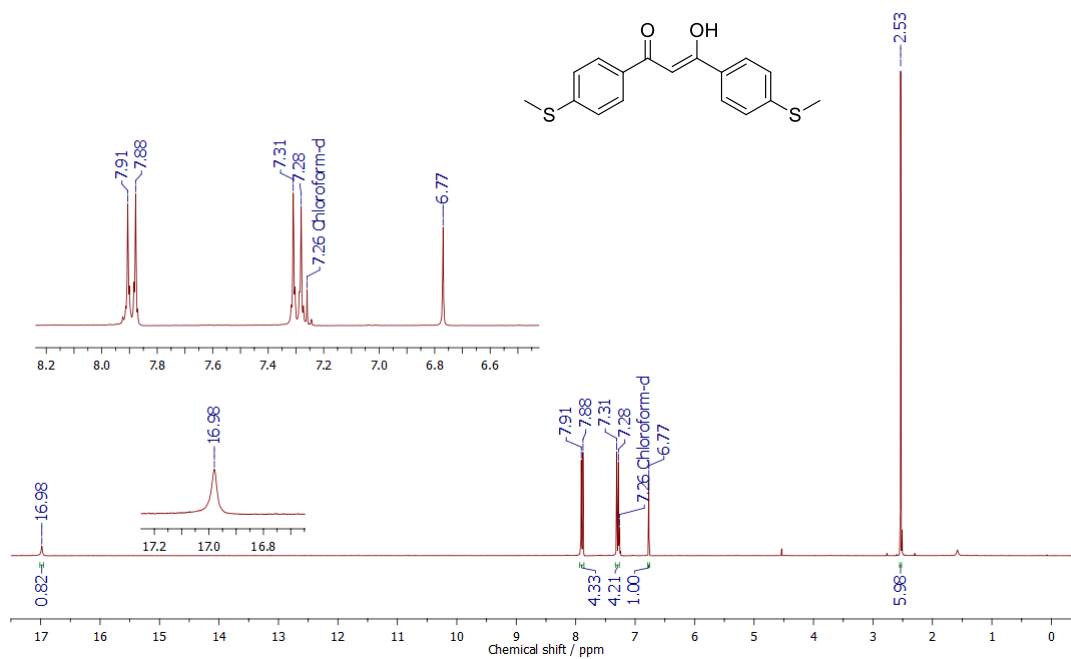


Figure S15. ^1H NMR spectrum of **6a** in CDCl_3 at 293 K.

^{13}C NMR (75 MHz, CDCl_3) δ 184.91, 145.12, 131.97, 127.61, 125.50, 92.33, 15.07.

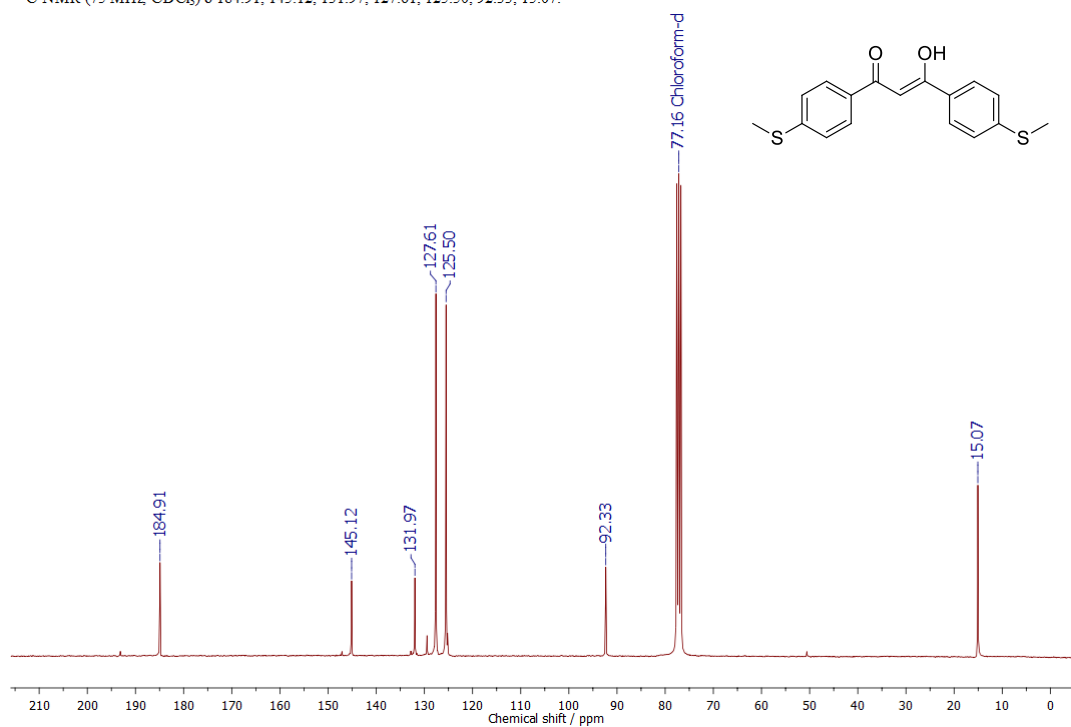


Figure S16. ^{13}C NMR spectrum of **6a** in CDCl_3 at 293 K.

^1H NMR (300 MHz, CDCl_3) δ 8.03 (d, $J = 8.7$ Hz, 4H), 7.33 (d, $J = 8.7$ Hz, 4H), 7.07 (s, 1H), 2.57 (s, 6H).

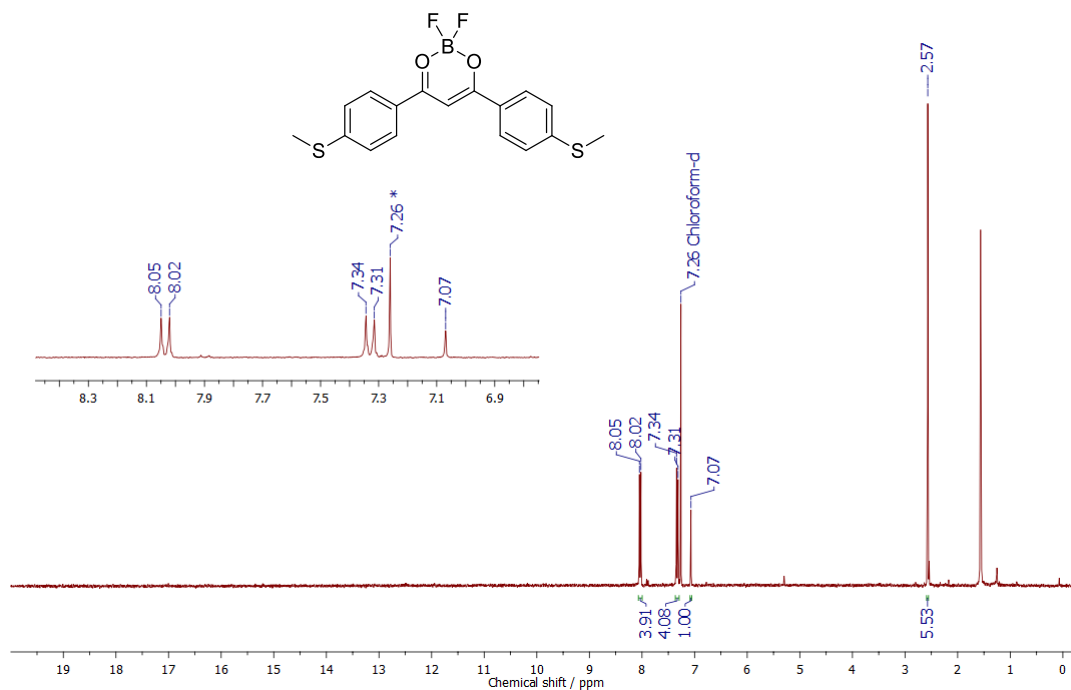


Figure S17. ^1H NMR spectrum of **6** in CDCl_3 at 293 K.

^{13}C NMR (101 MHz, CDCl_3) δ 181.47, 149.75, 129.20, 128.05, 125.31, 92.38, 14.78.

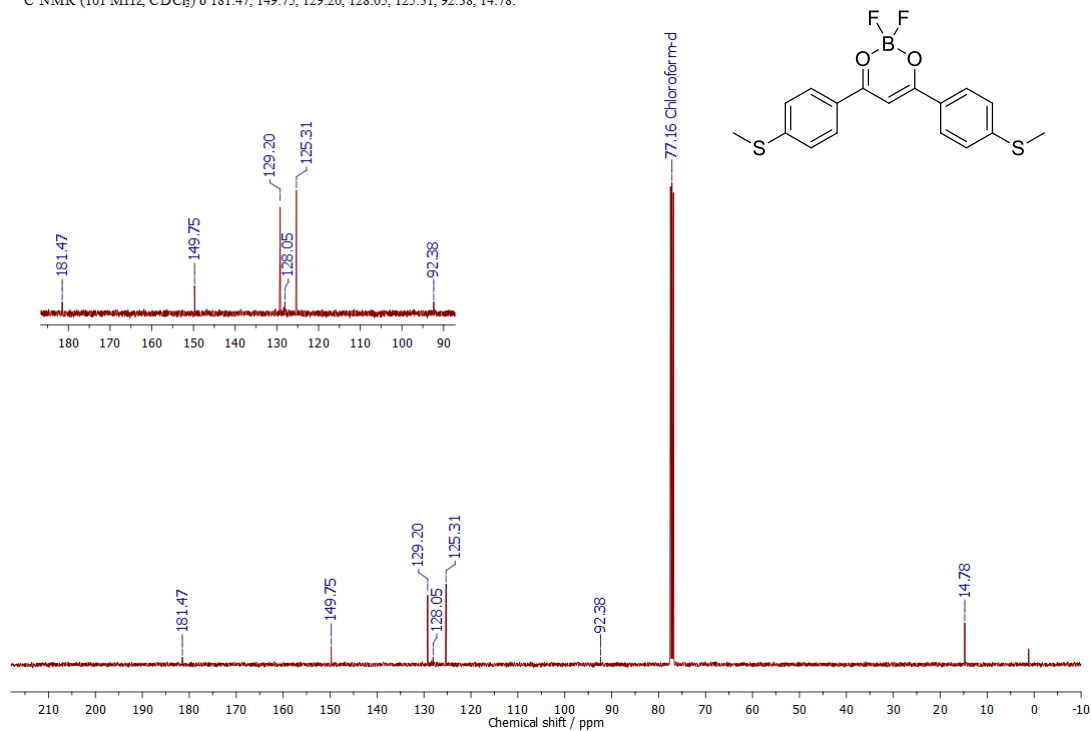


Figure S18. ^{13}C NMR spectrum of **6** in CDCl_3 at 293 K.

¹⁹F NMR (235 MHz, DMSO) δ -140.86, -140.92.

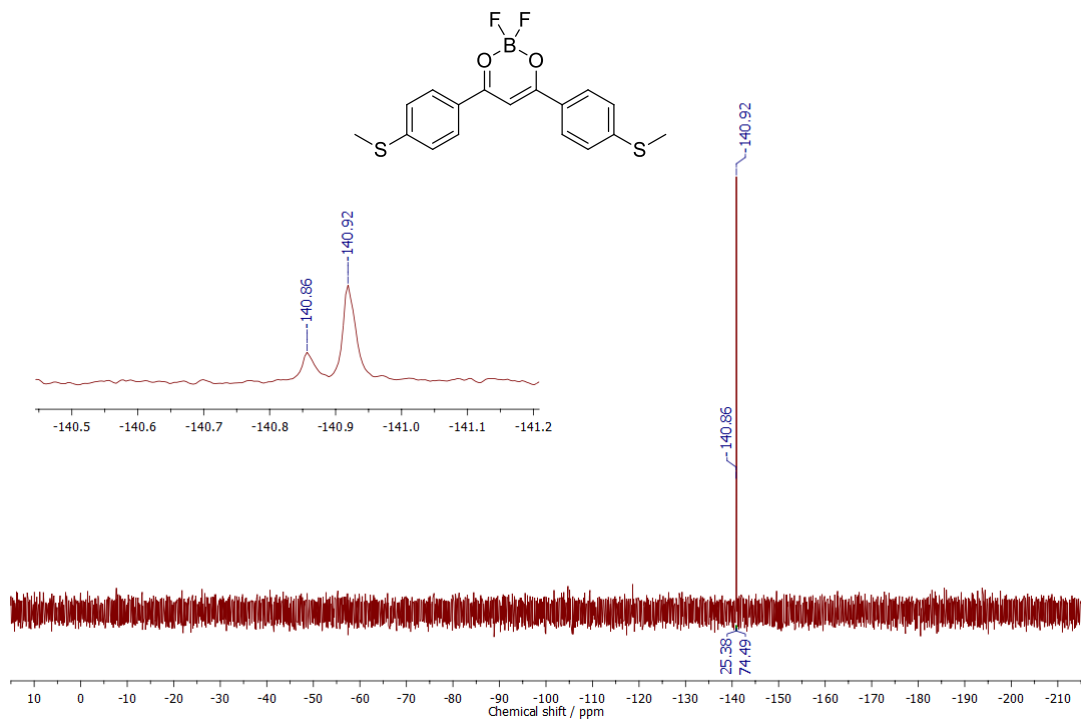


Figure S19. ¹⁹F NMR of **6** in DMSO-d₆ at 298 K.

6. FTIR Spectra

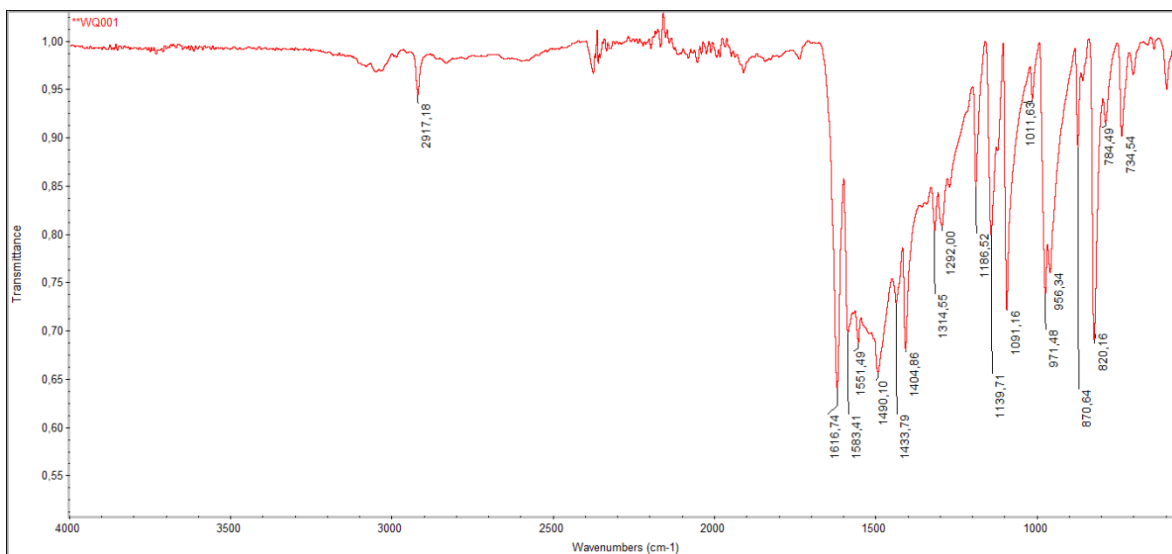


Figure S20. FTIR spectrum of 1.

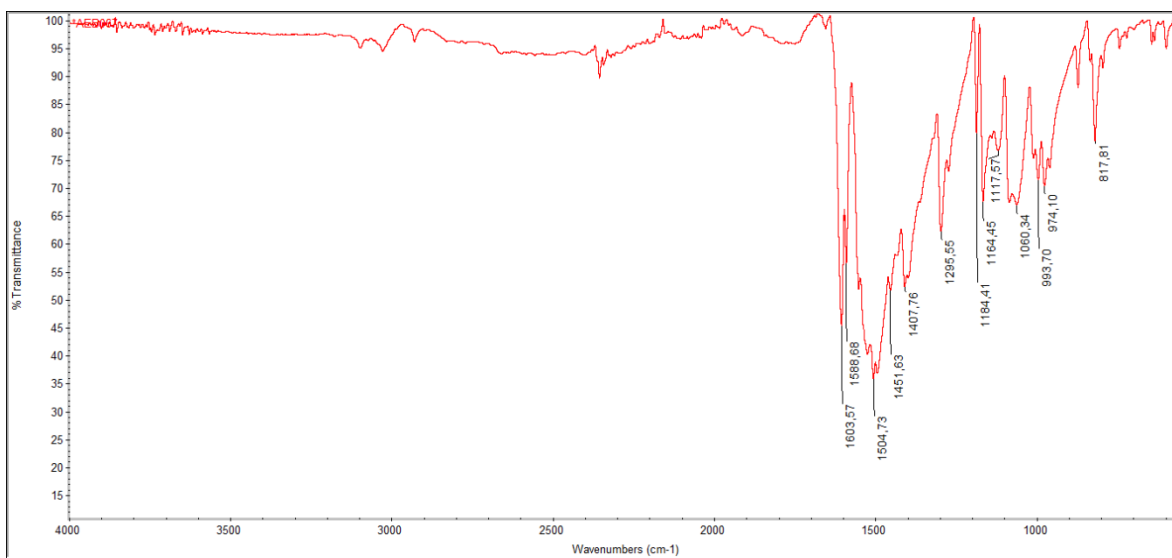


Figure S21. FTIR spectrum of 2.

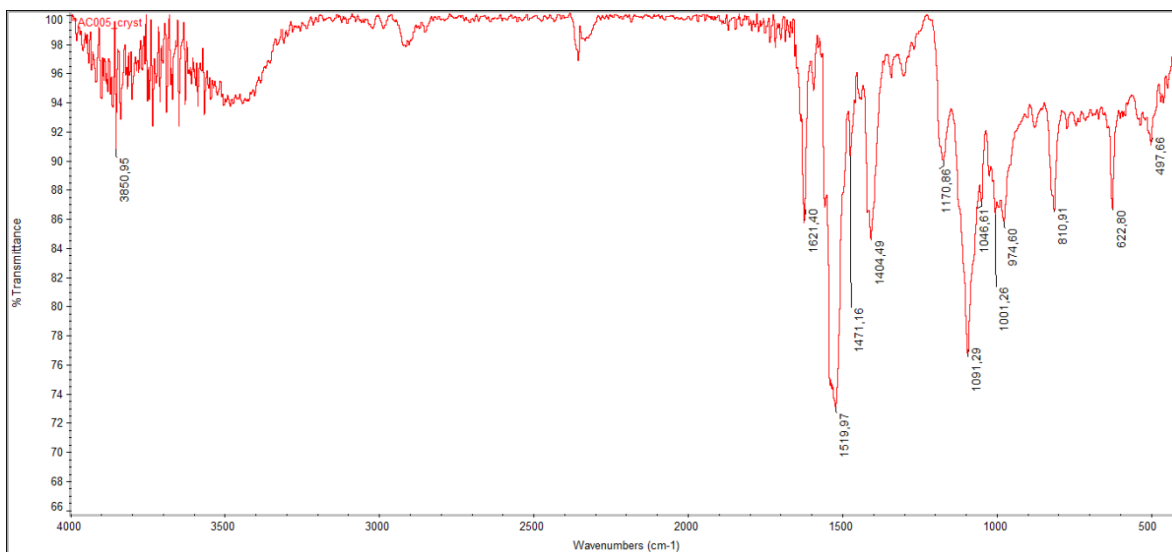


Figure S22. FTIR spectrum of **3**.

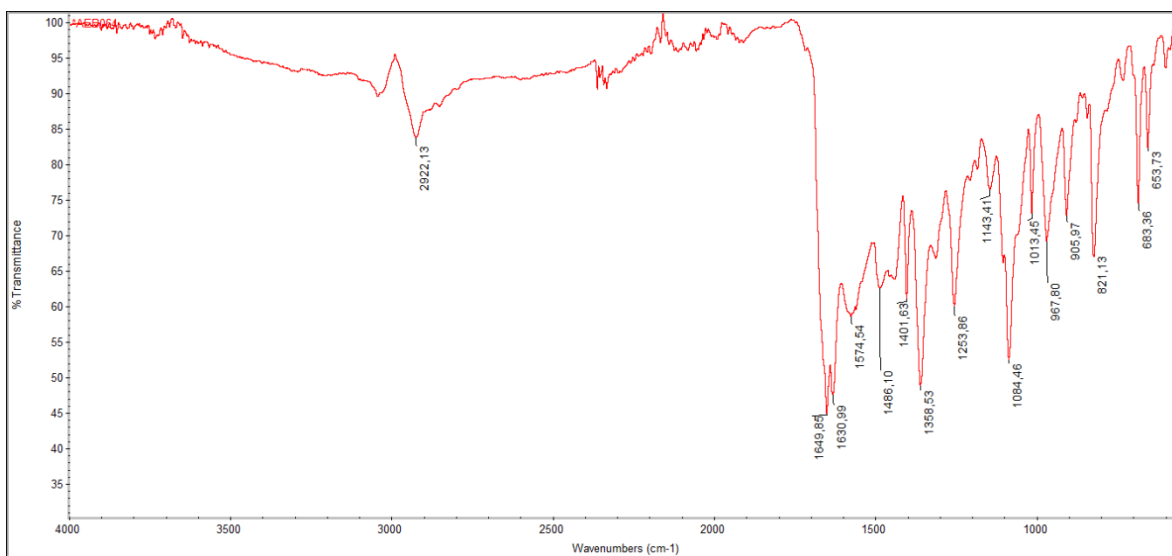


Figure S23. FTIR spectrum of **4a**.

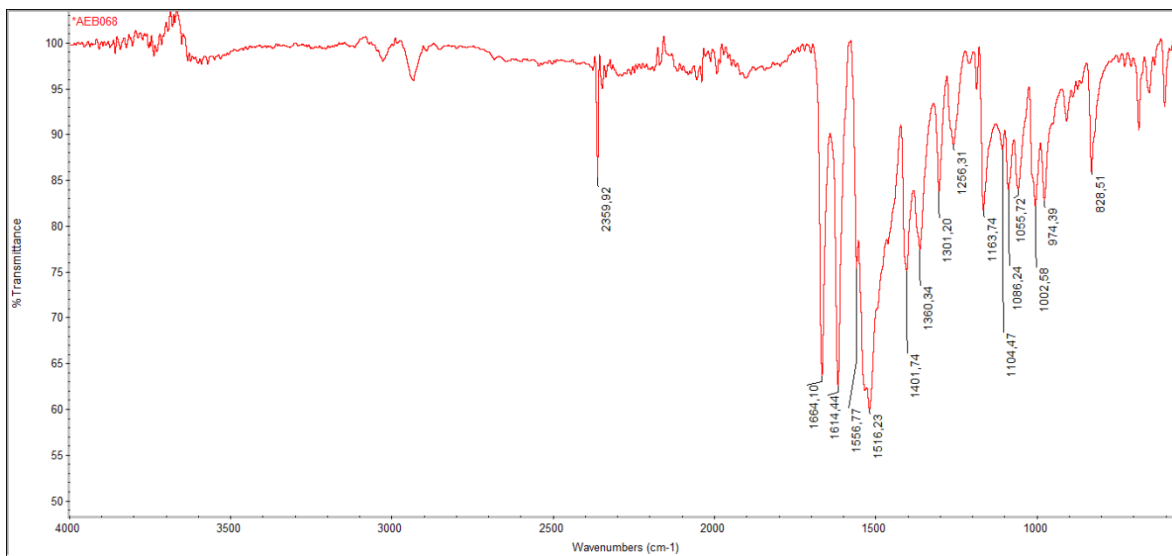


Figure S24. FTIR spectrum of 4.

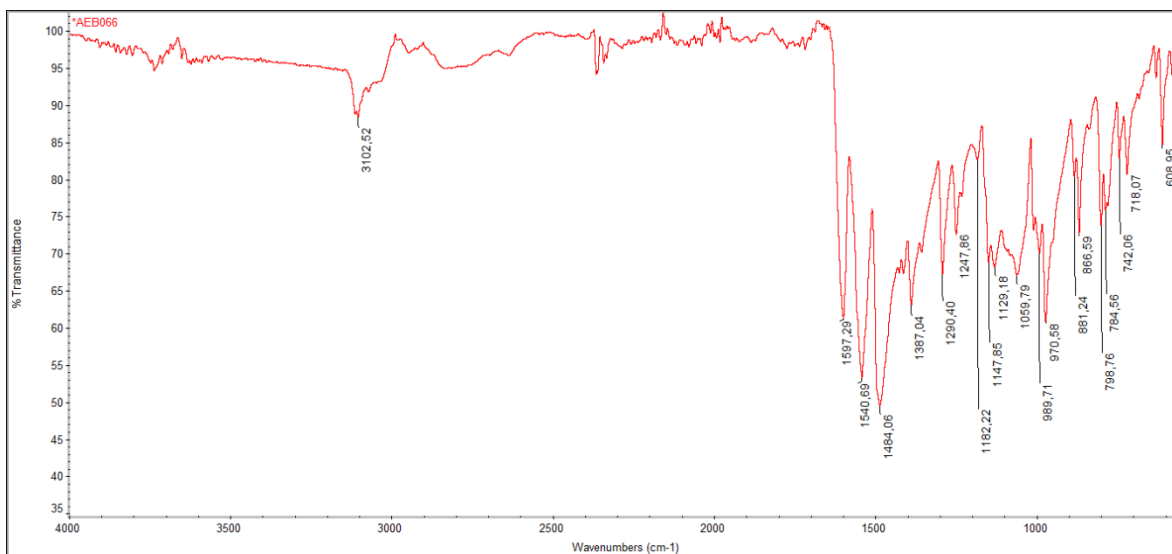


Figure S25. FTIR spectrum of 5.

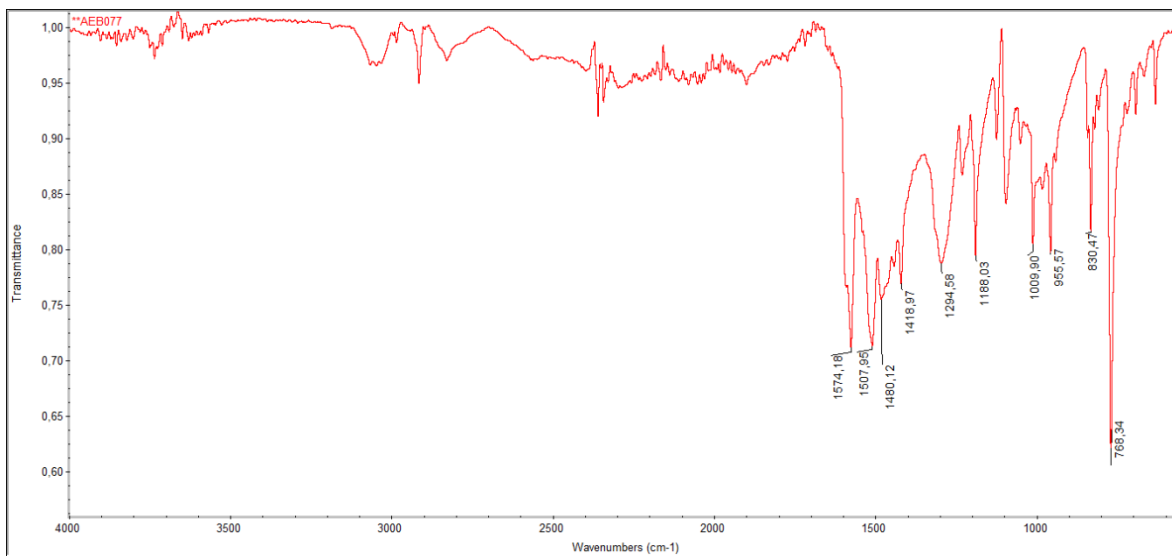


Figure S26. FTIR spectrum of **6a**.

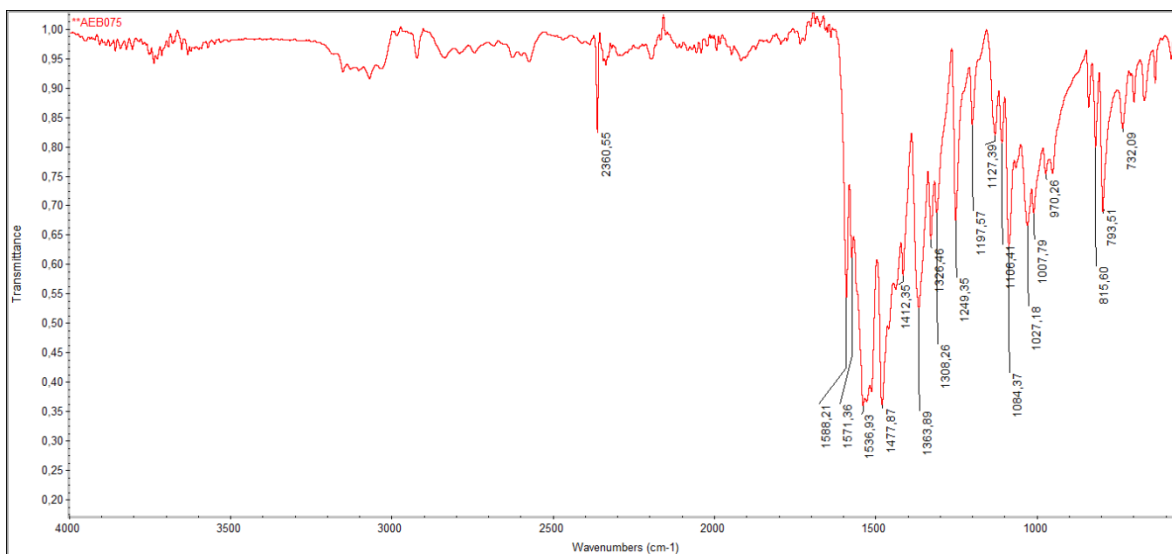


Figure S27. FTIR spectrum of **6**.

7. UV-Vis Diffuse Reflectance Spectra

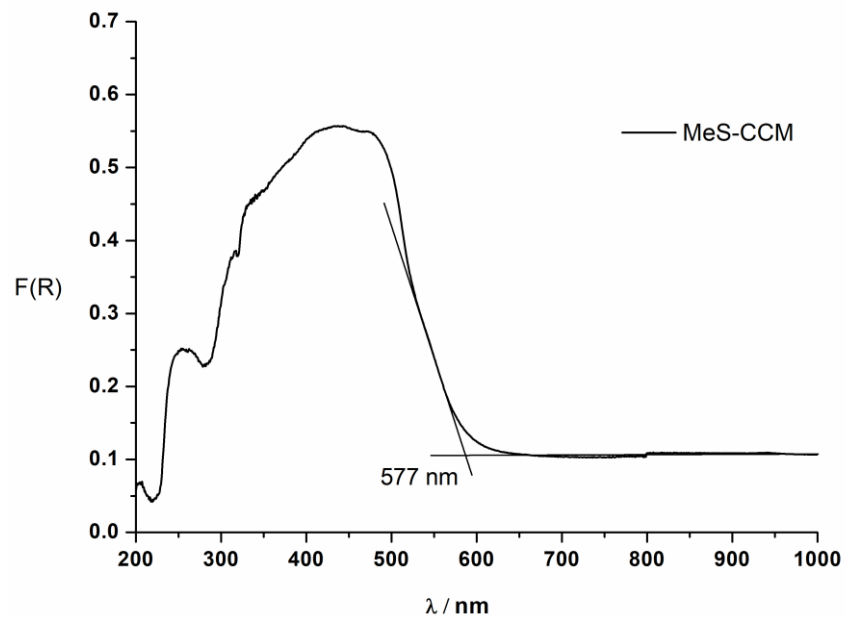


Figure S28. UV-Vis Diffuse Reflectance spectrum of **1**.

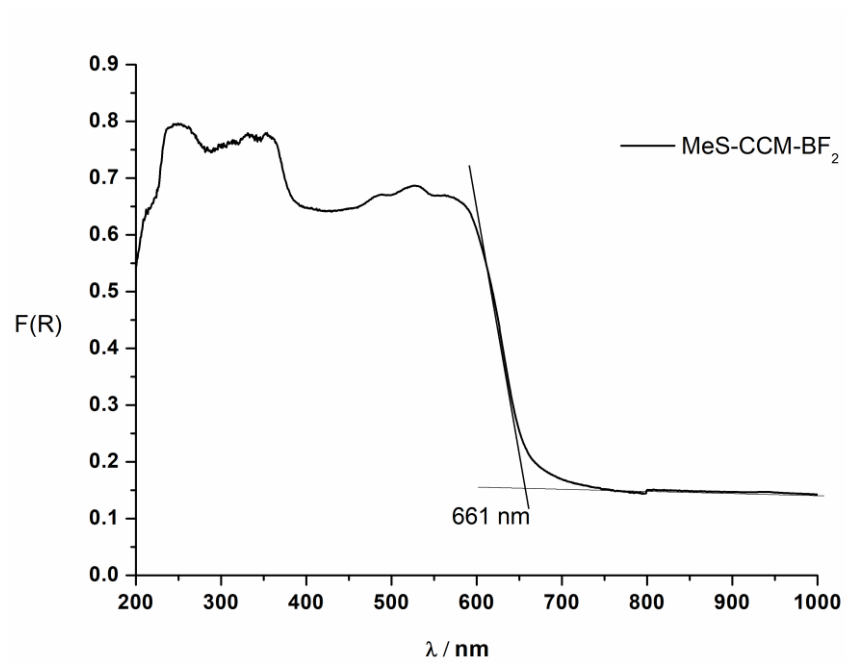


Figure S29. UV-Vis Diffuse Reflectance spectrum of **2**.

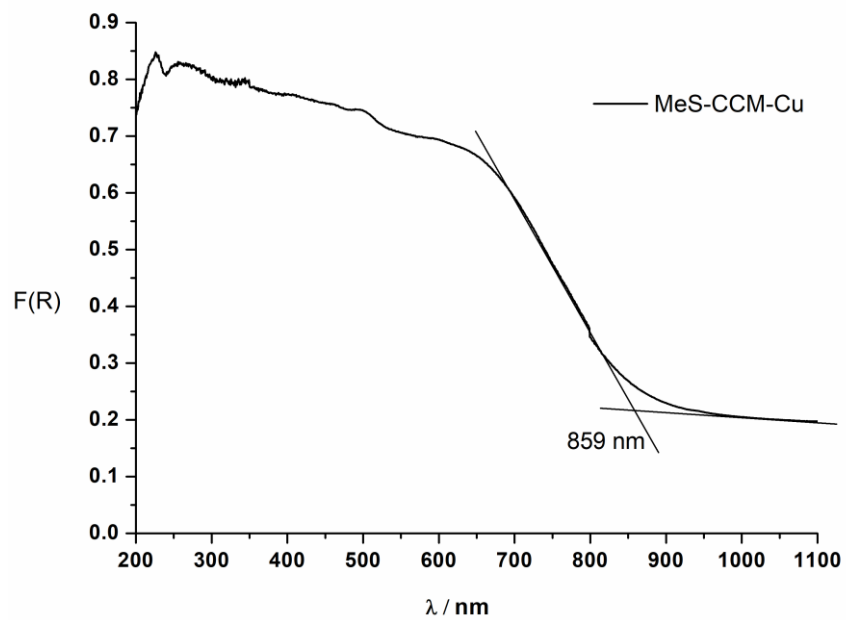


Figure S30. UV-Vis Diffuse Reflectance spectrum of **3**.

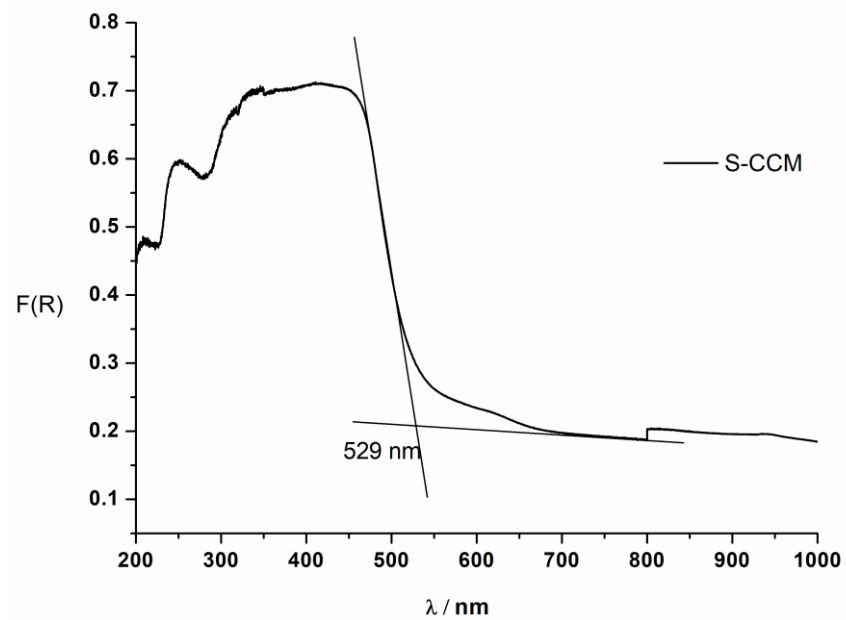


Figure S31. UV-Vis Diffuse Reflectance spectrum of **4a**.

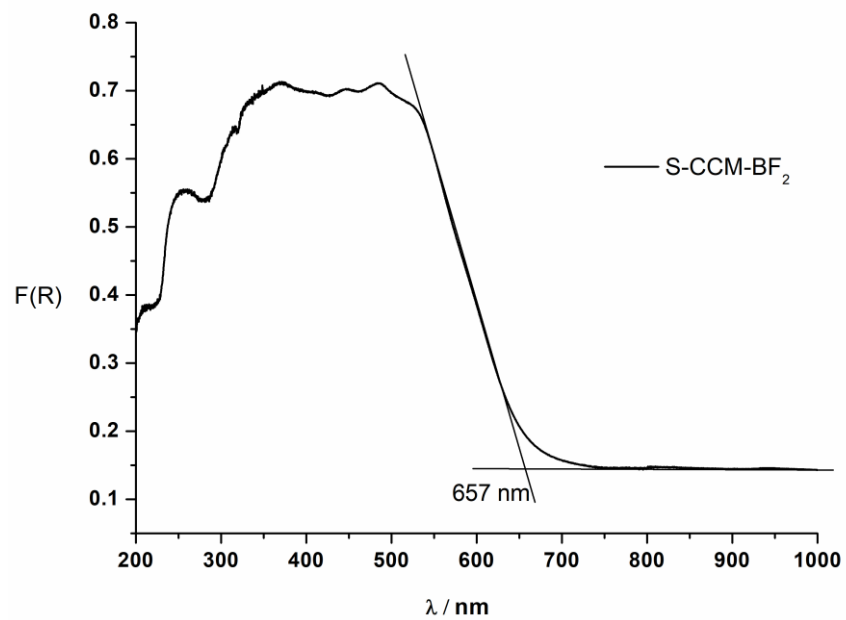


Figure S32. UV-Vis Diffuse Reflectance spectrum of 4.

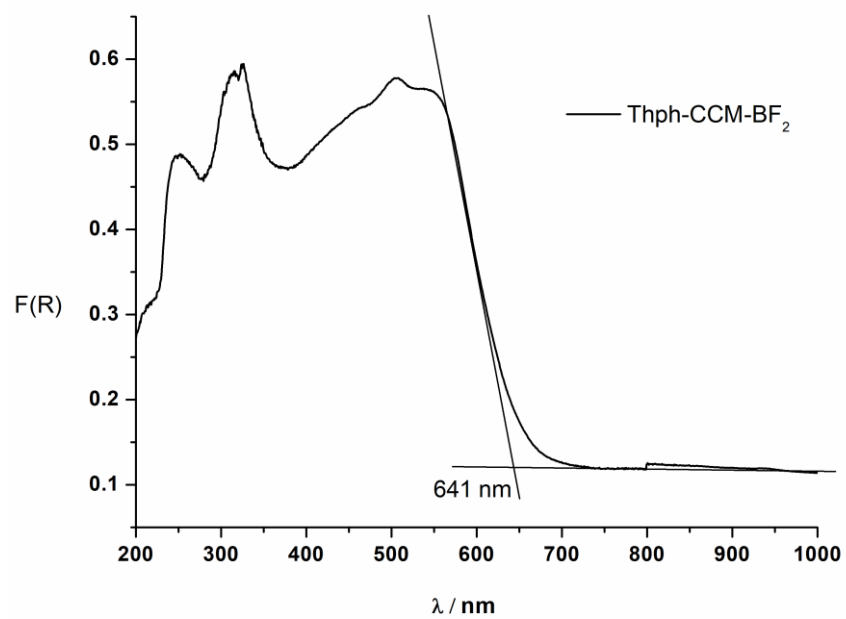


Figure S33. UV-Vis Diffuse Reflectance spectrum of 5.

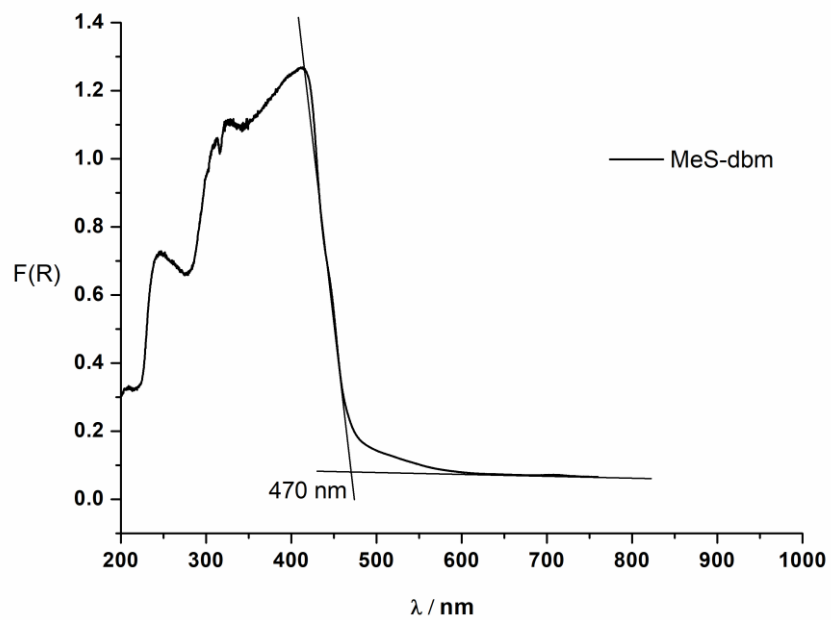


Figure S34. UV-Vis Diffuse Reflectance spectrum of **6a**.

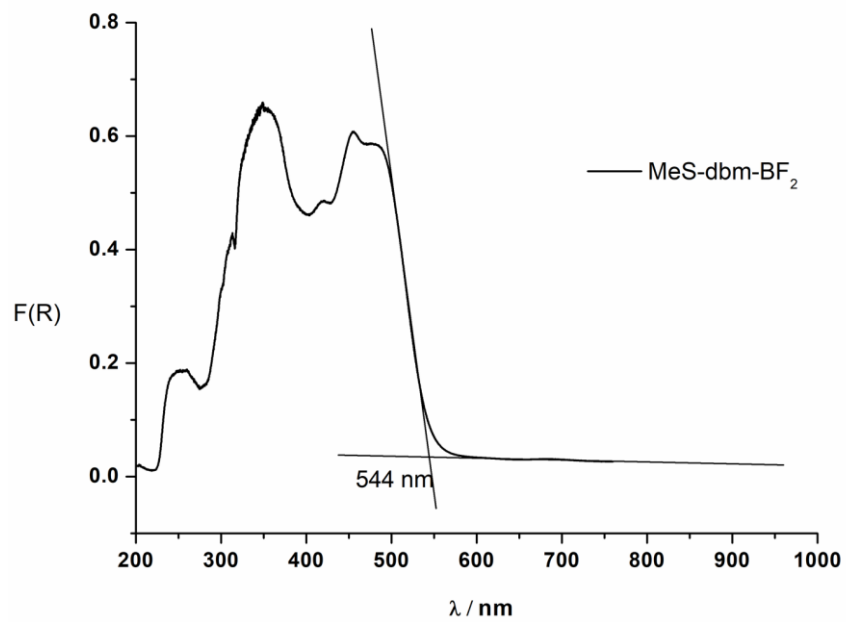


Figure S35. UV-Vis Diffuse Reflectance spectrum of **6**.

8. Cyclic Voltammetry (CV) and Differential Pulse Voltammetry (DPV)

Measurements were conducted under Ar, in dry CH_2Cl_2 containing 0.1 M tetrabutylammonium hexafluorophosphate [TBA(PF₆)] as supporting electrolyte. Potentials vs. Fc/Fc⁺

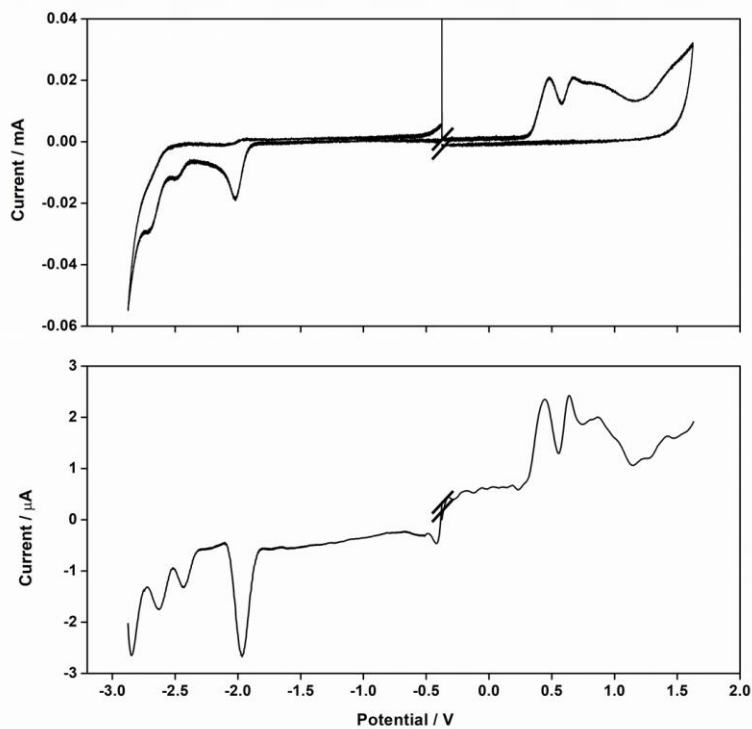


Figure S36. CV and DPV of **1** scanning of the oxidation and reduction windows respectively.

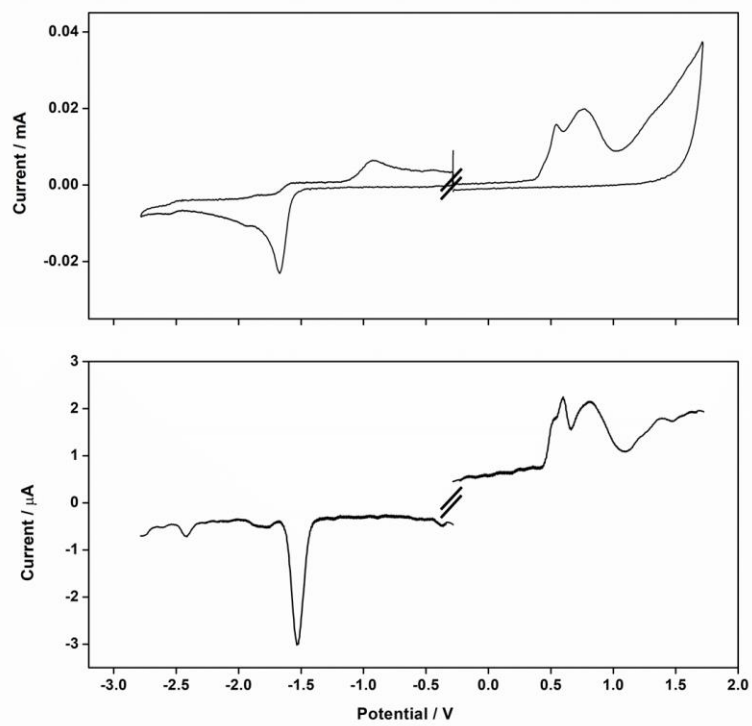


Figure S37. CV and DPV of **2** scanning of the oxidation and reduction windows respectively.

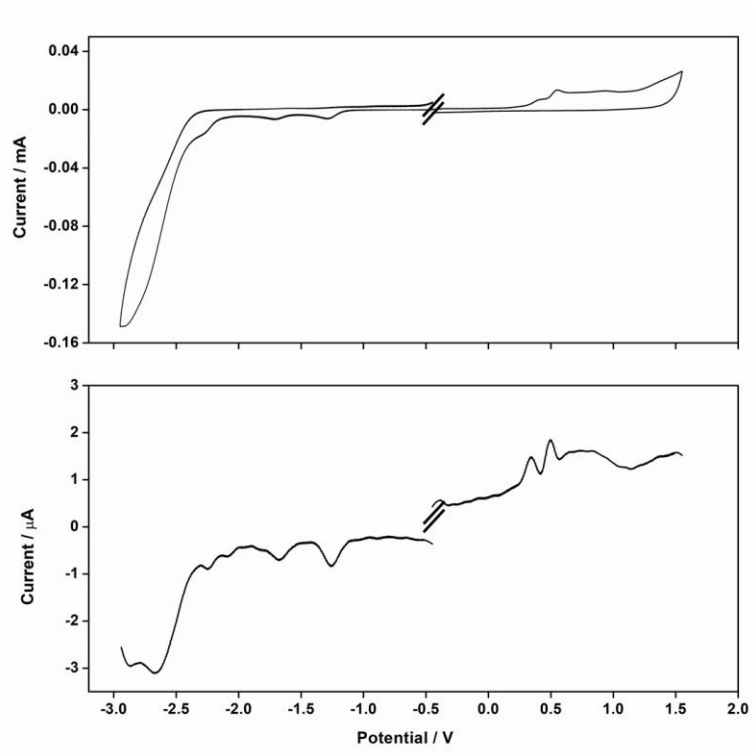


Figure S38. CV and DPV of **3** scanning of the oxidation and reduction windows respectively.

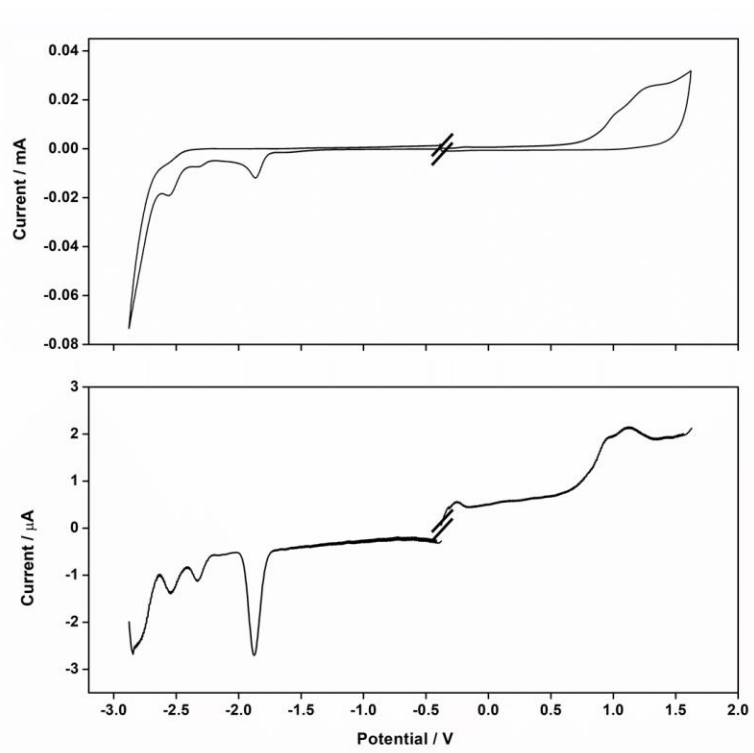


Figure S39. CV and DPV of **4a** scanning of the oxidation and reduction windows respectively.

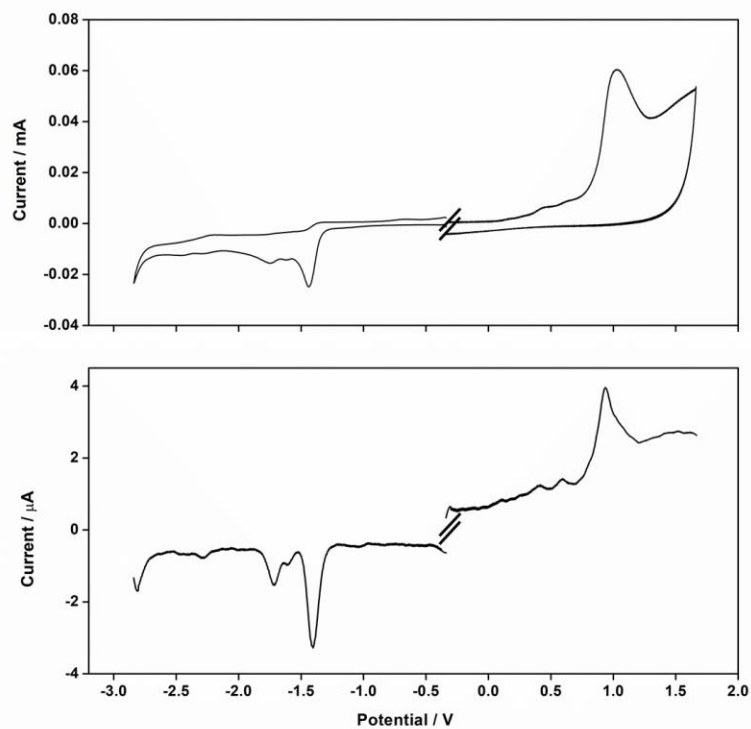


Figure S40. CV and DPV of **4** scanning of the oxidation and reduction windows respectively.

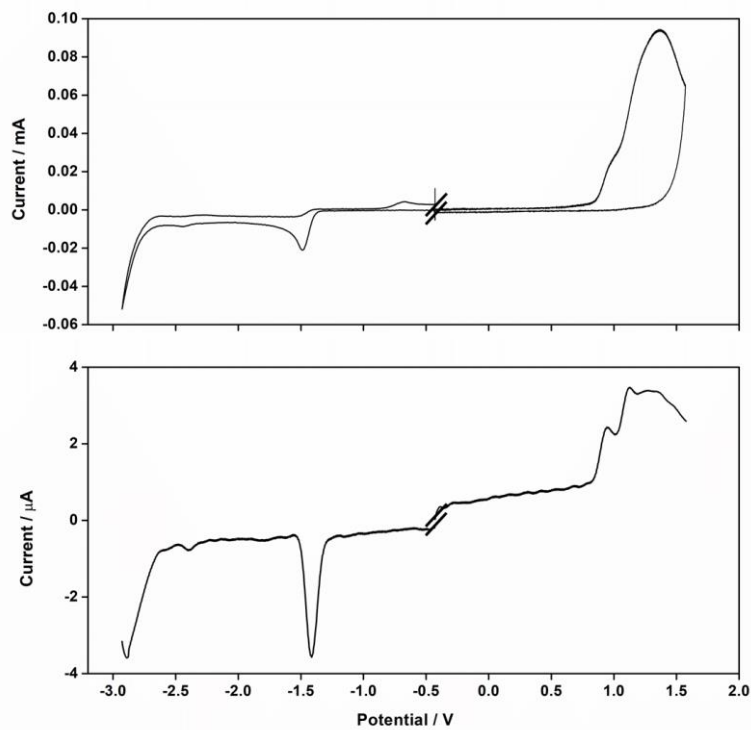


Figure S41. CV and DPV of **5** scanning of the oxidation and reduction windows respectively.

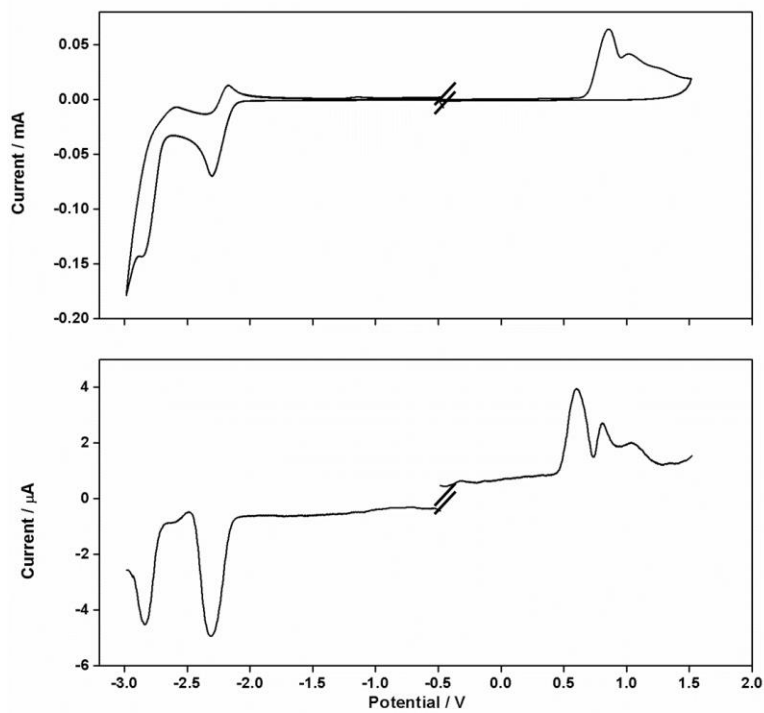


Figure S42. CV and DPV of **6a** scanning of the oxidation and reduction windows respectively.

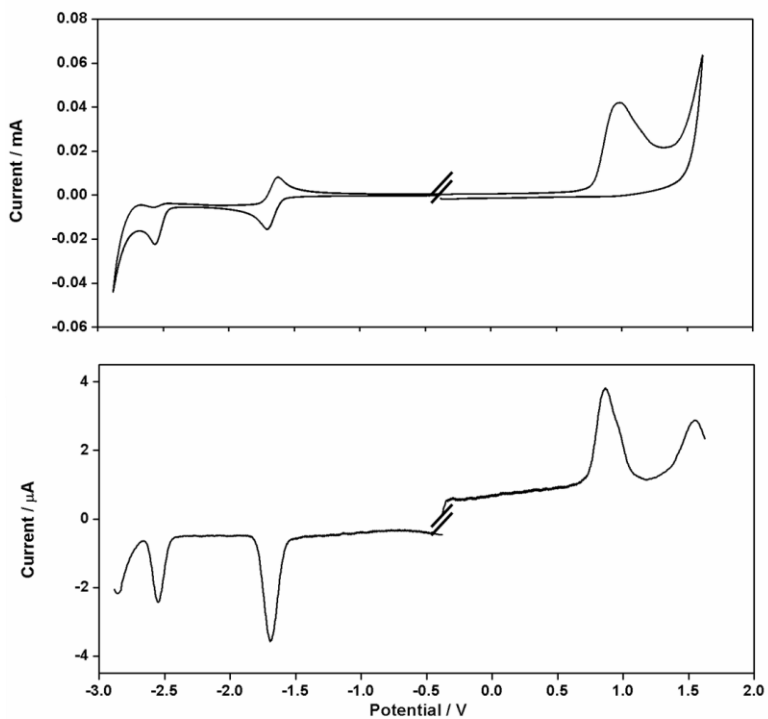


Figure S43. CV and DPV of **6** scanning of the oxidation and reduction windows respectively.

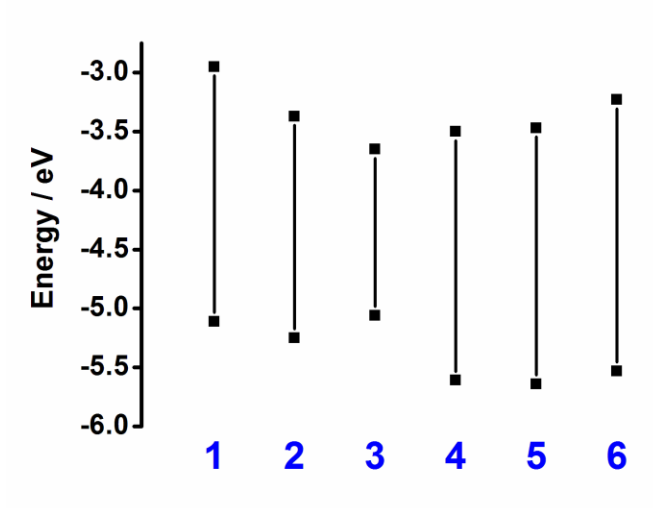


Figure S44. Energetic diagram: HOMO and LUMO orbital energy distribution for systems **1-6**.

9. Stability study in different solvents

^1H NMR of boron-curcuminoids in CD_2Cl_2 with days.

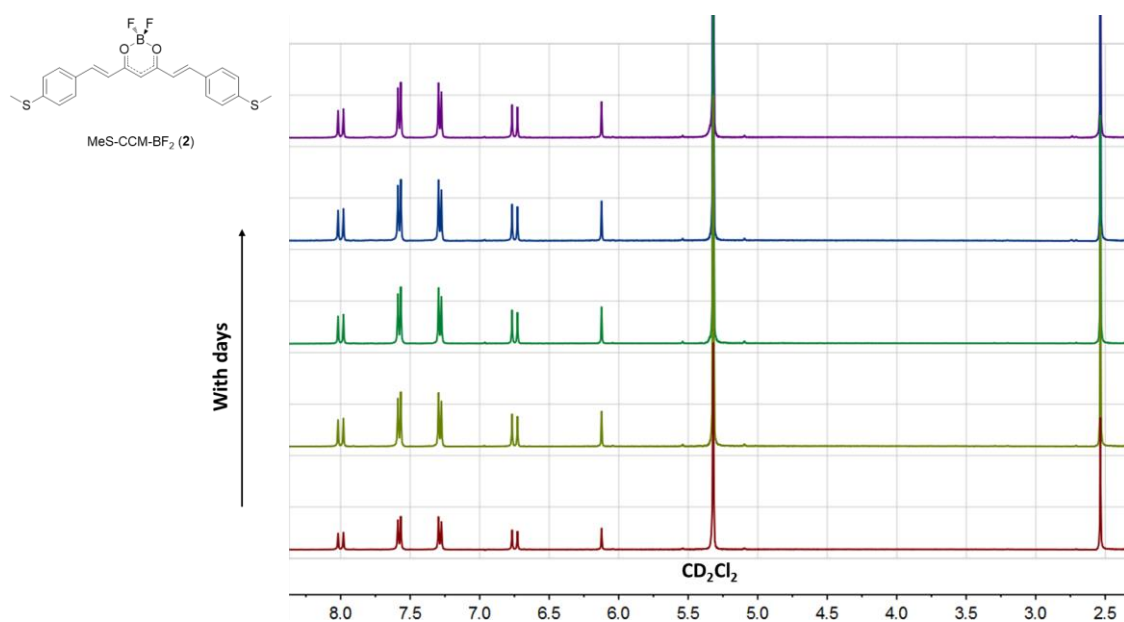


Figure S45. ^1H NMR of **2** in CD_2Cl_2 with days.

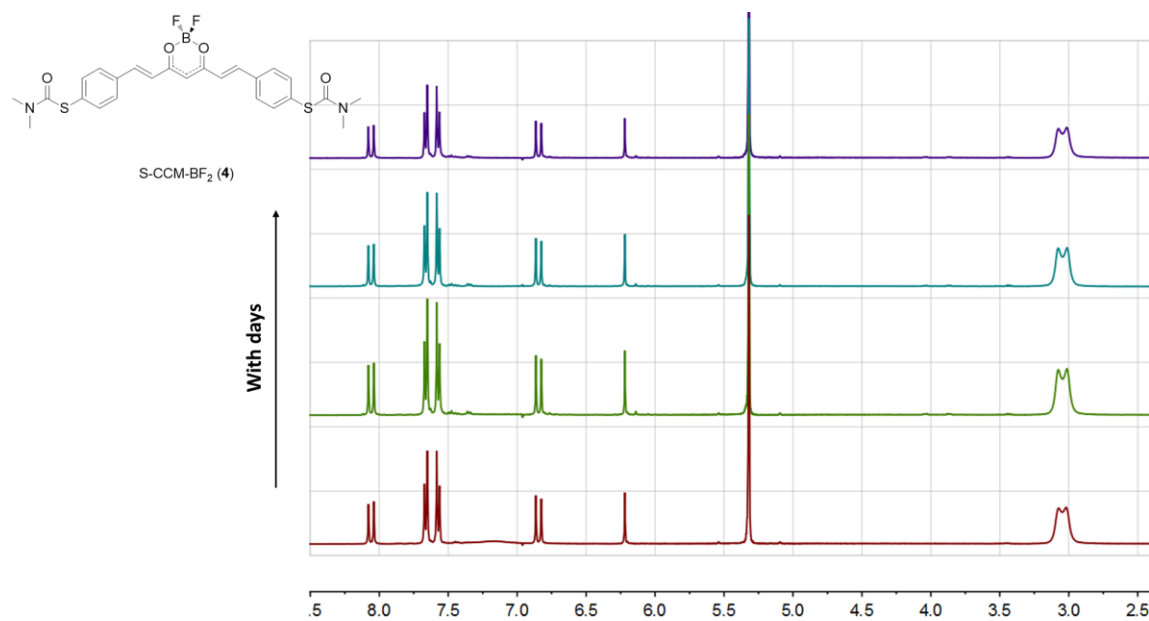
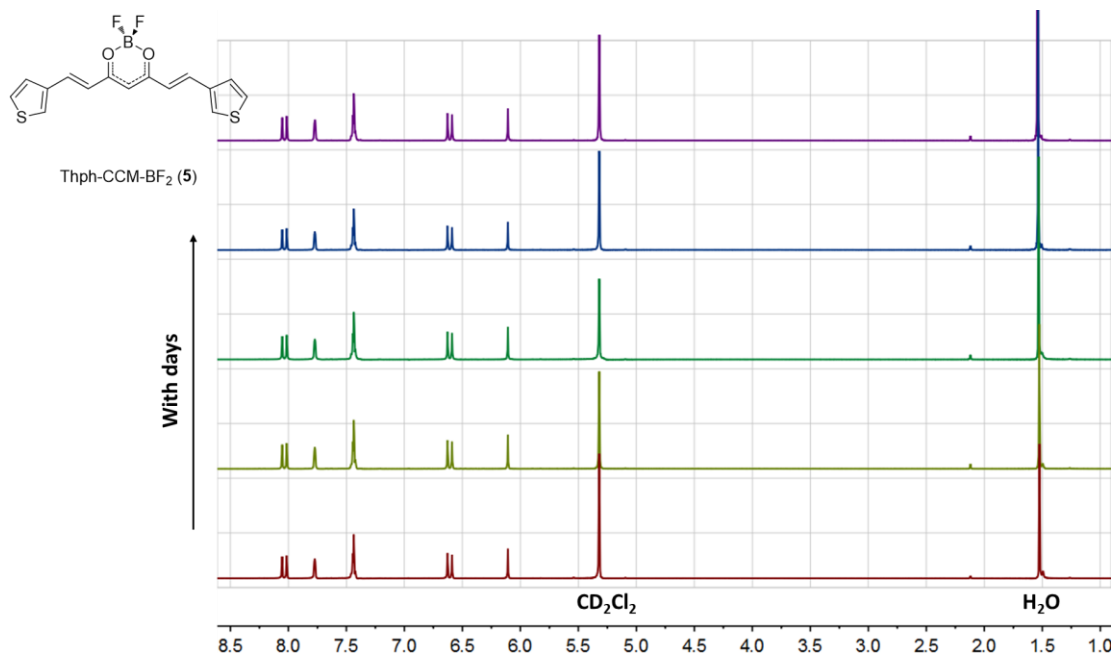
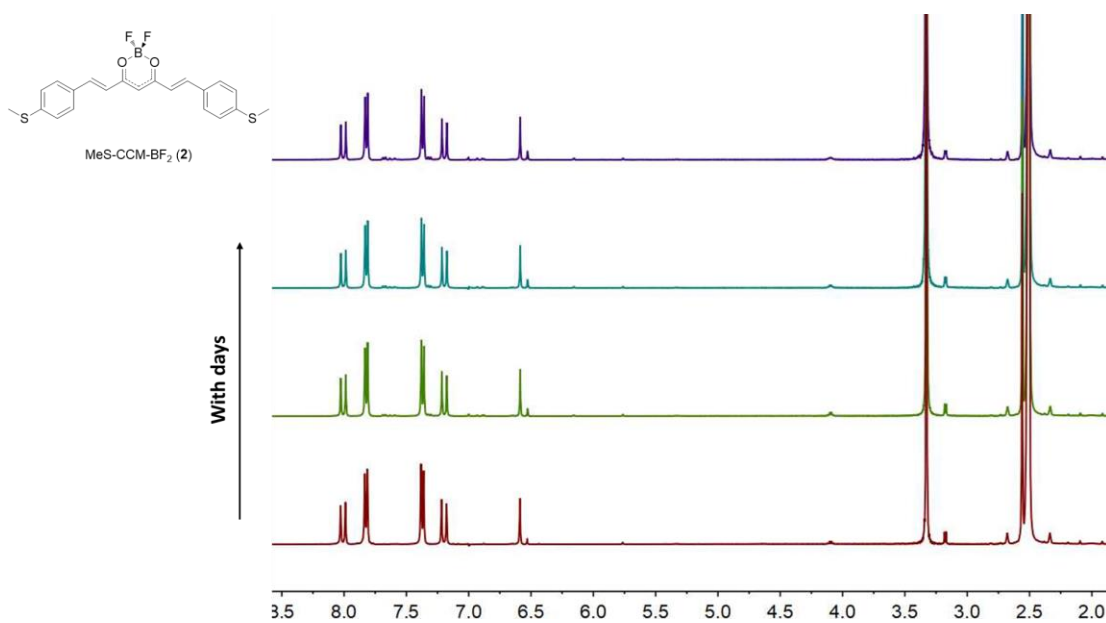


Figure S46. ^1H NMR of **4** in CD_2Cl_2 with days. The experiment was performed without deprotecting the sides of the compound.



¹H NMR of boron-curcuminoids in DMSO-d₆ with days.



^1H NMR of boron-curcuminoids **2** in CD_2Cl_2 (5 mM) under different temperature.

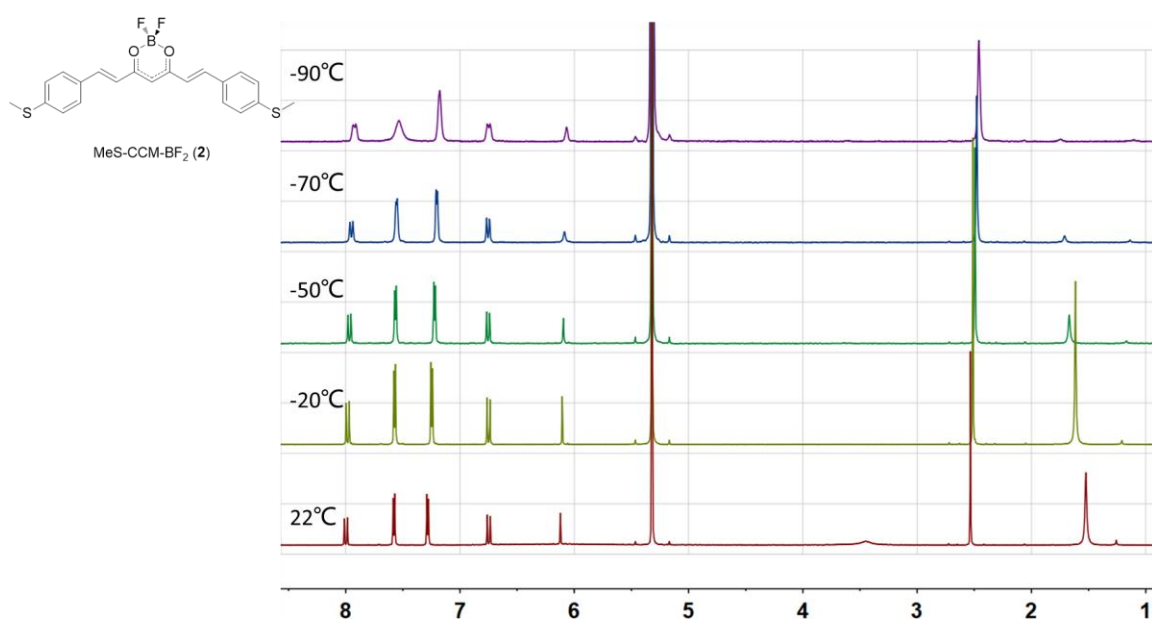


Figure S49. ^1H NMR of **2** in CD_2Cl_2 under different temperature.

10. MCBJ methodology

Mechanical break junction devices consist of a phosphorus bronze flexible substrate coated with a thin insulating layer of polyimide on top of which a narrow gold wire is lithographically patterned. A narrow constriction (width of ≈ 100 nm) in the middle of the wire is suspended using reactive ion etching. The sample is then clamped at both ends and subsequently bent by the action of a pushing rod beneath the centre of it. The bending causes the gold wire to stretch and, eventually, to break. In this process two atomically sharp electrodes are formed and can be re-fused and broken again thousands of times with sub Ångström precision.⁴

During the breaking process, the conductance ($G = I/V$) is recorded using a logarithmic amplifier. A breaking trace is recorded by measuring the conductance value as a function of the electrode displacement from the metallic regime to the noise level of the electronics. Traces are aligned in such a way that zero displacement is defined as the point where the metallic contact is lost and the conductance drops sharply below the conductance quantum ($G_0 = 2e^2/h$), where e is the electron charge and h is Planck constant). The data is displayed in the form of two-dimensional (2D-) conductance vs. displacement histograms, in which the colour code represents the relative frequency a particular conductance value is measured at the corresponding displacement value. The actual distance between the electrodes is larger than the one displayed in the 2D-histogram because the electrodes snap like a rubber band when the last atom loses contact. On average, the retraction of the electrodes after breaking is about 0.5 nm,⁴ and this distance should be added to the distances displayed in the 2D-histograms.

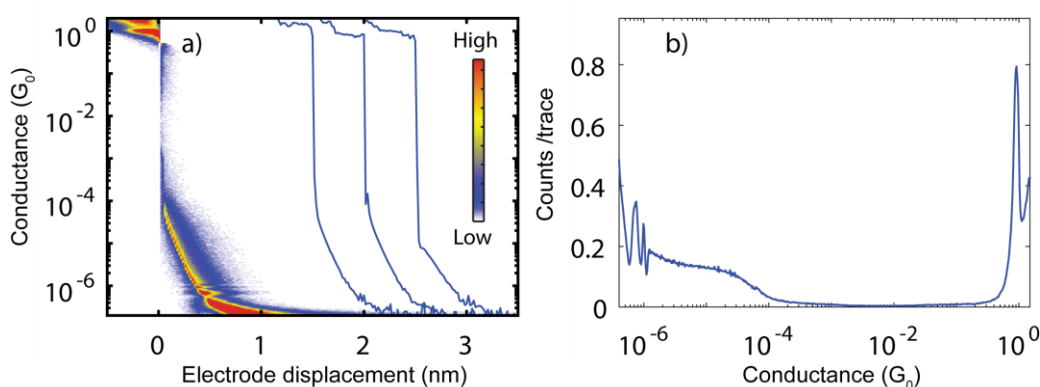


Figure S50. a) Blue lines correspond to three representative breaking traces from a bare gold sample (offset in the x-direction for clarity). The coloured data on the left represents a two-dimensional conductance vs. electrode displacement histogram of a MCBJ constructed from 10000 consecutive traces measured in a sample before depositing the molecule of interest. b) One-dimensional (1D) conductance histogram of the same measurement obtained by integration along the x-axes of the histogram in a). The peak at $1 G_0$ at the right hand side correspond to a single gold atom contact.

As stated in the main text, the data of a conductance measurement with a molecule contain a mixture of empty and molecular traces (traces in which a molecule was trapped between the electrodes). In order to get a better estimation of the molecular conductance it is convenient to split the data: the criterion used to select the data is based on the way the conductance decay as the electrode displacement increases. When a molecule bridges the gap this dependence is weaker than that of one empty trace.

A breaking trace is considered 'molecular' if there is a window of $\Delta x = 0.5$ nm in the section of positive electrode displacement that has an average decay rate greater than -0.5 decades/nm, where the decay rate is defined as the slope of the linear fit to $\log_{10}(G(x))$. On average the decay rate of a bare gold (clean) sample is -4 decades/nm and the threshold of -0.5 produces false positive labelling below 1% of the traces. This criterion allows for an unbiased way to split the data and define the yield of molecular junction as the ratio of the number of molecular traces over the total amount of traces. In Figure S52b the 2D-conductance vs. electrode displacement histograms of compounds **1** to **6** constructed from only traces labelled as molecular are displayed. There the plateau-like characteristics are more dominant than in the cases where all the data is included.

Systematic measurements were performed in compounds **1** and **3** in the same manner as for compound **2** (Figure S51) but no indication of a double-peak structure is observed, in Figure S51 shows the 1D-conductance histograms of measurements at different bias voltages constructed from the selected traces out of 2000 consecutive traces. The measurement strongly suggests that the presence of two characteristic conductance states in close proximity to each other is a feature originating from the boron difluoride (BF_2) group.

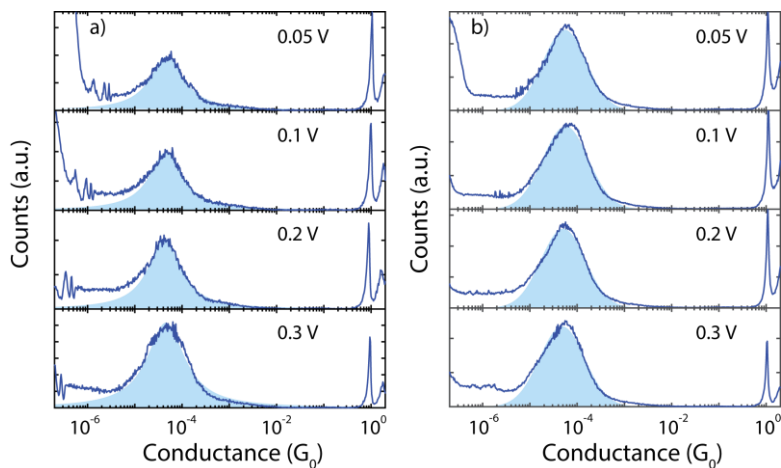


Figure S51. Series of 1D-conductance histograms of a single junction measured for bias voltages as indicated in the labels. Light blue shaded areas represent fits of log-normal distributions to the data in the region for which molecular features are seen for a) **1** and b) **3**. No clear indication of a double-peak structure is observed.

Figure S52a display the 2D-conductance vs. electrode displacement histogram of the six molecules considered in this study. The region characterizing the molecular features of **2** is broader along the entire plateau length than those of the other molecules, while in the case of compound **4** the molecular plateau becomes wider towards the end of the traces (around 2 nm). This latter observation indicates that the broadening of the conductance peak originates from a change in the anchoring configuration or the extension of the molecule inside the gap, but not from a bi-stability observed for compound **2**. The 1D-conductance histograms of representative samples of the six compounds are presented in Figure S53a. They were constructed from the selected traces of the measurements displayed in Figure S52. The light blue areas correspond to log-normal fits used to obtain the conductance values reported in the main text.

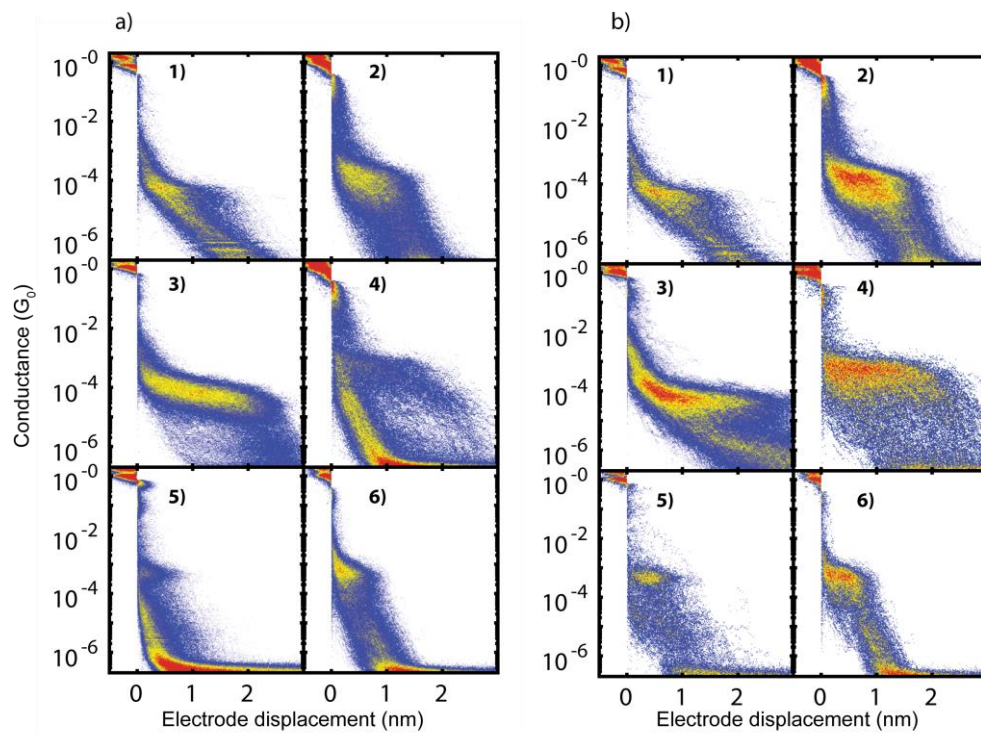


Figure S52. 2D-conductance vs. electrode displacement histograms of compounds **1** to **6** as indicated by the labels constructed from a) 2000 consecutive traces and b) from molecular traces selected by the filtering method described previously using the same dataset as in a).

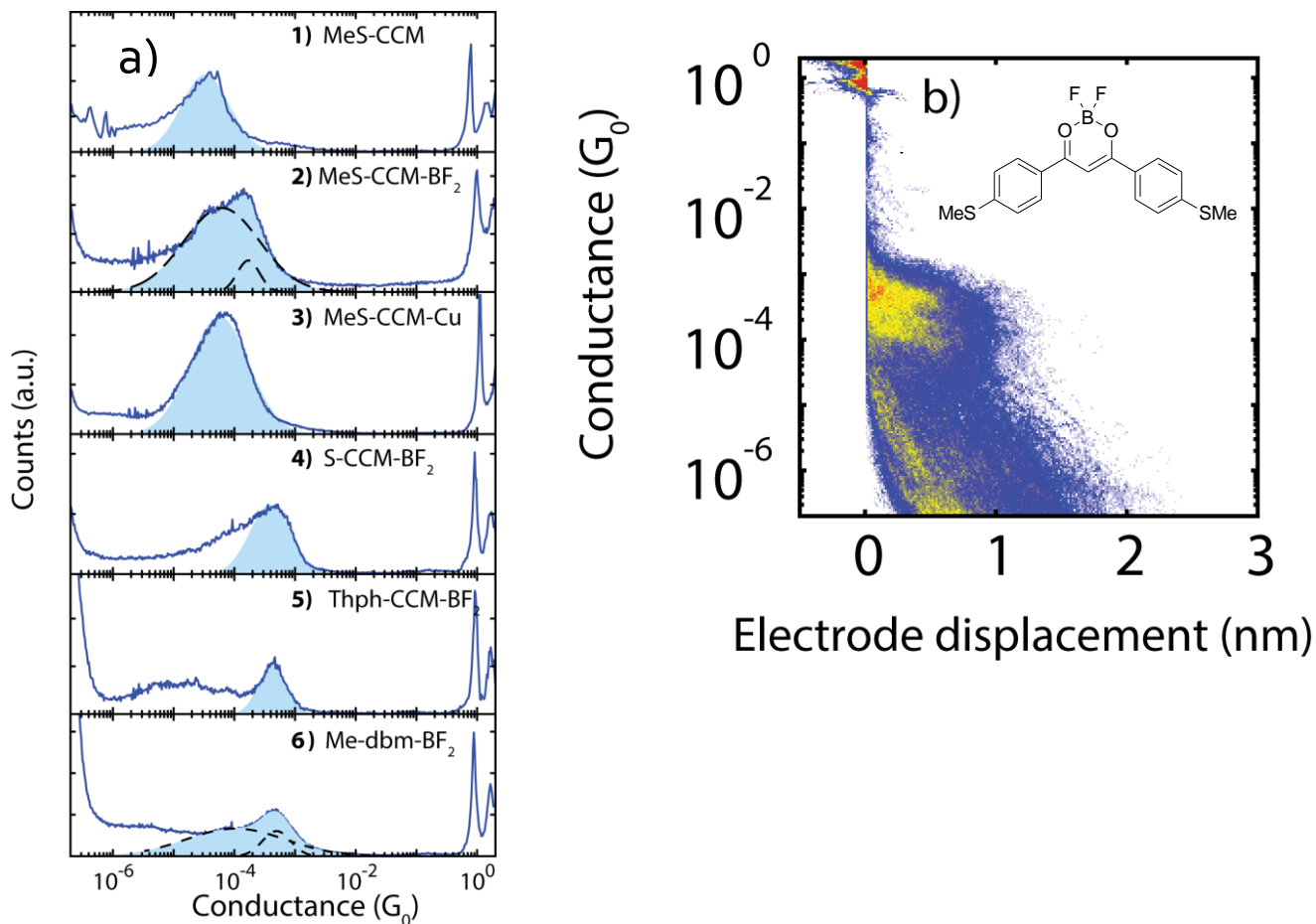


Figure S53. a) 1D-conductance histograms of compounds **1** to **6** constructed from the traces considered in the selected histograms of Figure S52.

The presence of two peaks in the case of compound **6** in Figure S53 may not be obvious, but measurements at a slower electrode speed (0.3nm/s) and a bias voltage of 0.25 V makes this feature clearer as seen in Figure S54b. The switching behavior of between these two conductance states is also visible in individual traces and some examples are displayed in Figure S54a.

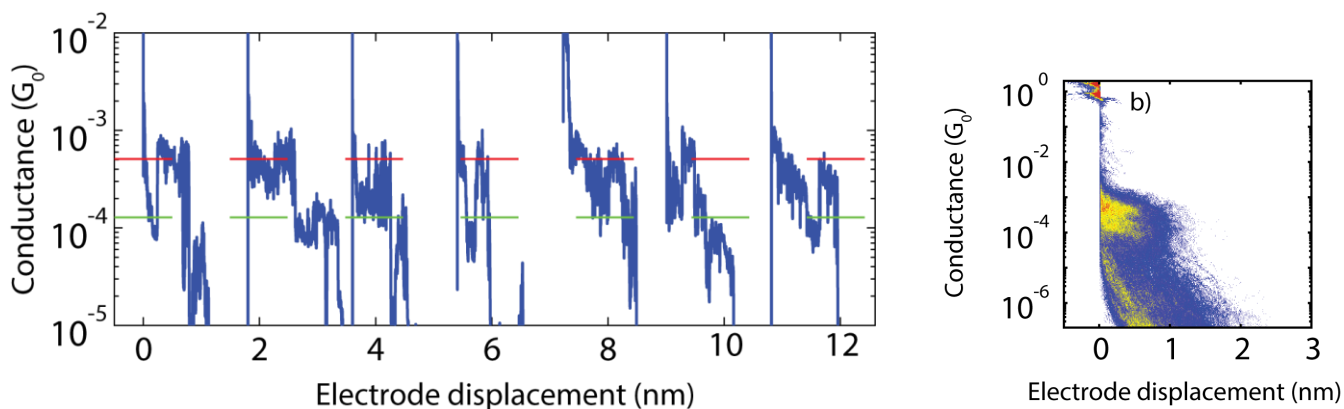


Figure S54. Series of single breaking traces of MeS-dbm-BF₂ (**6**) measured at a bias voltage of 0.2 V and an electrode speed of 0.3nm/s. Traces have been off set in the x-direction for clarity. b) 2D conductance vs. electrode displacement histogram constructed from 2000 consecutive traces of **6** of a measurement at an electrode speed of 0.3 nm/s and a bias voltage of 0.25 V (inset shows the molecular structure of **6**).

In conclusion, the experimental data strongly suggest that the appearance of two characteristic conductance states and a switching behaviour between them is related to the combination of MeS anchoring groups and a Boron difluorine (BF₂) moiety attached to the central part of the molecule.

11. Theoretical studies

DFT and post Hartree-Fock calculations of the isolated molecules

Table S7. Total energies (in a.u.) and relative stabilization energies (in kcal/mol) for the different conformers of the three studied molecules (MeS-CCM-BF₂ (**2**), MeS-CCM (**1**) and MeS-CCM-Cu (**3**)). The structures were optimized at B3LYP-D3 and MP2 levels and the DLNPO-CCSD(T) energies were determined by using the B3LYP-D3 and MP2 optimized geometries. In bold is highlighted the most stable conformer for each molecule, for the DLNPO-CCSD(T) all optimized geometries DFT+MP2 were considered. In some cases, the result of the optimization geometry is a different conformer than the initial one, in such cases, it is indicated in the Table the final conformer.

MeS-CCM-BF₂ (**2**)

	B3LYP+D3-opt	CCSD(T) (DFT)	MP2-opt	CCSD(T) (MP2)
<i>flat</i>	-1983.58902466 14.9	-1980.325604059 0.5	<i>perp0</i>	-
<i>flat0</i>	-1983.58982386 14.4	-1980.326426311 0.0	<i>perp0</i>	-
<i>perpflat</i>	-1983.61284574 0.0	-1980.319716186 4.2	-1979.01288149 0.0	-1980.320186020 0.9
<i>perpflat0</i>	<i>flat0</i>	-	<i>perp180</i>	-
<i>perp0</i>	<i>flat</i>	-	-1978.99285845 12.6	-1980.321529160 0.1
<i>perp180</i>	<i>flat</i>	-	-1978.99287006 12.6	-1980.321607937 0.0

MeS-CCM (**1**)

	B3LYP+D3-opt	CCSD(T) (DFT)	MP2-opt	CCSD(T) (MP2)
<i>flat</i>	-1759.39108913 0.4	-1756.454103734 2.1	<i>perp180</i>	-
<i>flat0</i>	-1759.39167151 0.0	-1756.457499814 0.0	<i>perp0</i>	-
<i>perpflat</i>	<i>flat</i>	-	-1755.27738403 0.0	-1756.454133367 0.4
<i>perpflat0</i>	<i>flat0</i>	-	-1755.26504179 7.7	-1756.454721435 0.0
<i>perp0</i>	<i>flat0</i>	-	-1755.266530216 6.8	-1756.452668404 1.2
<i>perp180</i>	<i>flat</i>	-	-1755.26685632 6.6	-1756.453525075 0.7

MeS-CCM-Cu (**3**)

	B3LYP+D3-opt	CCSD(T) (DFT)
flat	-3747.02810540 0.03	-3742.580391779 0.1
flat0	-3747.02815633 0.0	-3742.580466780 0.0
perpflat	<i>flat0</i>	-
perpflat0	-3747.02814160 0.0	-3742.539682767 25.6
perp0	<i>flat</i>	-
perp180	<i>flat</i>	-

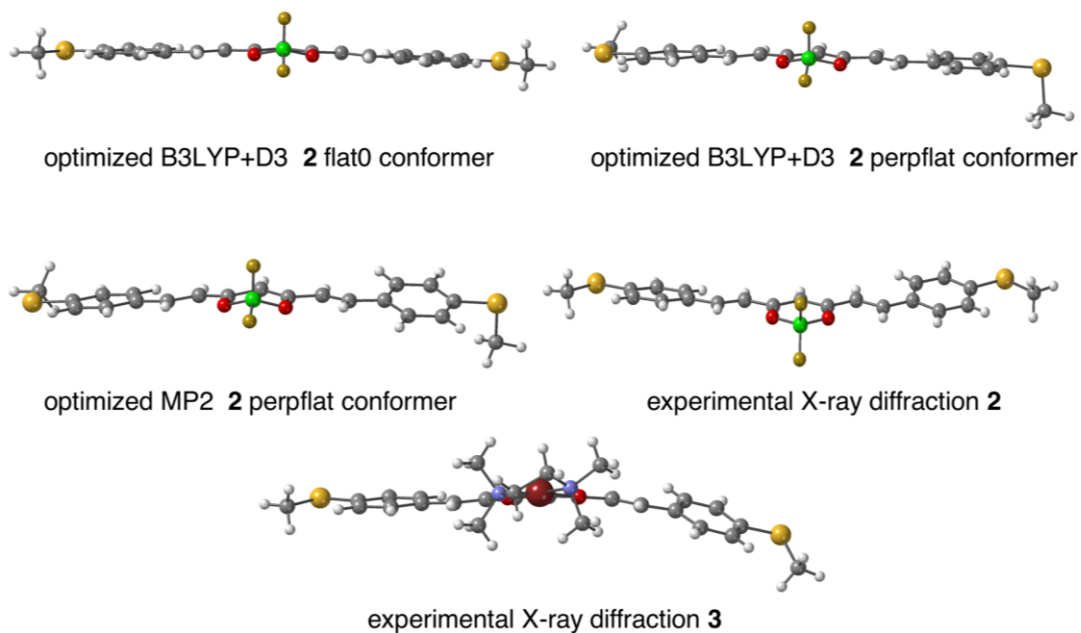


Figure S55. Comparison of the optimized structures of the *flat0* and *perpflat* conformer of the MeS-CCM-BF₂ molecules at B3LYP-D3 with the *perpflat* conformer at MP2 levels. Experimental structure of the molecules **2** (CSD refcode RUXFIB) and **3** obtained by X-ray diffraction. DFT provides structures with a flat central moiety while MP2 gives unrealistic non-flat structures. Experimentally, the molecules have the tendency to be flat but packing interactions considerably distort some parts of the molecule as it is shown in the available **2** and **3** experimental structures.

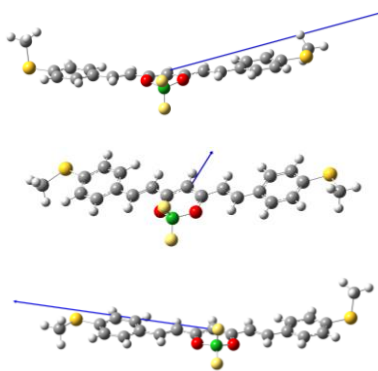


Figure S56. Dipolar moment for the *perpflat* (left), *flat0* (center) and *perpflat0#* (right) conformers for the MeS-CCM-BF₂ (**2**). The dipolar moment values are respectively 22.9, 5.1 and 22.9 Debye.

Periodic DFT calculations including two gold electrodes

Periodic DFT calculations were performed using fhi-aims code¹³ using numerical basis set of “light” quality for the geometry optimization and a single-point energy of the optimized geometry with the “tight” basis set. The PBE functional¹⁴ was employed and a set of four k-points in the first Brillouin zone. A model unit cell was used using a 2D 4x4 gold superlattice with a gold tip for the contact with the molecule (see Figure S57). Full geometry optimization calculation (including cell parameters) was performed to analyze the stability of the conformers. In order to compare the total energies also the isolated molecules without the gold electrodes were optimized.

In this section, the results using a most simple DFT exchange-correlation functional as PBE instead of the hybrid functional employed in the previous sections indicate a preference for the isolated molecules for the flat conformer (very close in energy to those *flat0* predicted by the DLNPO-CCSD(T) method). The most remarkable conclusion of these calculations is that the interaction of the molecule with the gold electrodes also favors the change to a *perpflat* conformation. Such behavior is similar to that induced by an external electric field that also helps that the molecules adopt such conformations.

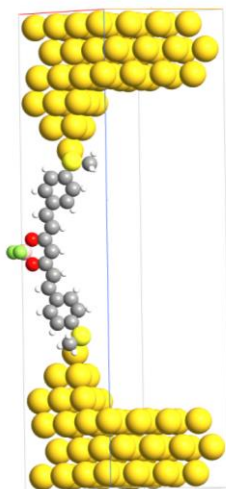


Figure S57. Optimized structure for the unit cell of the *perpflat* conformer of MeS-CCM-BF₂ (**2**) attached to the gold electrodes.

Table S8. Total energies (in a.u.) and relative stabilization energies (in kcal/mol) with numerical basis set “tight” using the optimized geometry with “light” basis set for periodic models similar to those of Fig S56 for compound **2** MeS-CCM-BF₂ and **1** MeS-CCM. The most stable system is highlighted in bold.

	MeS-CCM-BF ₂	MeS-CCM-BF ₂ -- gold	MeS-CCM	MeS-CCM -- gold
<i>flat</i>	-1982.06009197	-2074811.32532209	-1758.04662516	-2074587.31455260
	0.0	3.9	0.0	4.3
<i>flat0</i>	-1982.05969971	-2074811.31397887	-1758.04656447	-2074587.30821002
	0.25	11.1	0.04	8.2
<i>perpflat</i>	<i>flat</i>	-2074811.33165491	<i>flat</i>	-2074587.32134528
		0.0		0.0

DFT and MP2 calculations of the isolated molecules under and external electric field

In the main text the DFT results of the molecules have been discussed. At MP2 level (see Figure S58), qualitatively the results are similar to those obtained with DFT: the *perpflat* conformers keep their structure for the all calculated external electric fields while the *flat0* conformer transforms at low external electric fields ($10 \cdot 10^{-4}$ a.u.) in the *perpflat0* conformer. Hence, the main difference is that at MP2 level the transformation from the *flat0* to the *perpflat0* conformers it happens at lower fields than for DFT. Such results could be expected taking into account that the *perpflat0* conformers are quite stable using the MP2 method, thus, even small fields may be capable of inducing the change toward such flat structures (*perpflat0*). As before MP2 method seems to over-stabilize perpendicular structures in comparison with DFT or DLNPO-CCSD(T) methods and also the experimental data for compound **2** that adopts a *flat0* conformer in the crystal determined by X-ray diffraction.

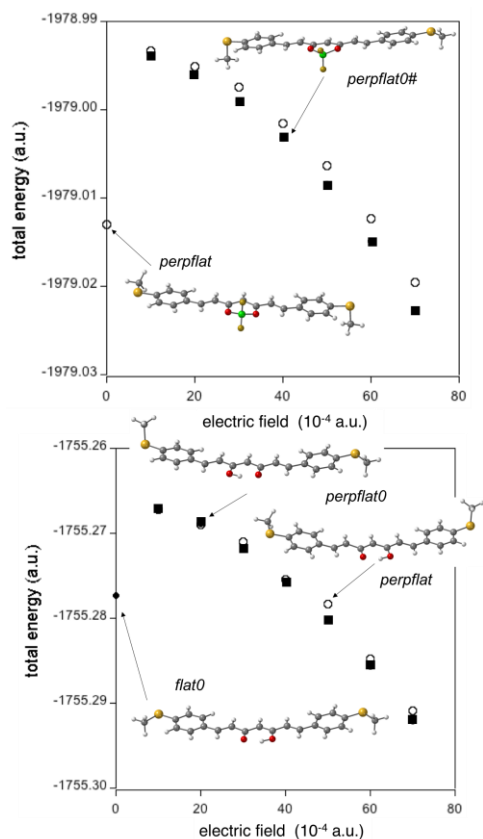


Figure S58. Total energy dependence with the electric field for the *perpflat* (white symbols) and *flat0* (black symbols only optimized at zero-field for MeS-CCM) conformers for the MeS-CCM-BF₂ (**2**, top) and MeS-CCM (**1**, bottom) molecules at MP2 level. Circle symbols indicate that the result of the geometry optimization is the same conformer than the initial geometry while square symbols indicate that there is a change of conformer due to the influence of the electric field. A new conformer appears for any electric field in the case of MeS-CCM-BF₂ with the perpendicular S-Me group in the same direction than the out-of-plane B-F bond (black squares in left Figure) that we will call *perpflat0#*

Table S9. Calculated conductance values (in G₀ units) for MeS-CCM (**1**), MeS-CCM-BF₂ (**2**), and MeS-CCM-Cu (**3**) obtained with the ATK code using the full consistent NEGF method and the PBE functional for different conformers of the three studied molecules.

	1	2	3
flat	0.36 10 ⁻²	1.6 10 ⁻²	2.0 10 ⁻²
flat0	0.83 10 ⁻²	2.2 10 ⁻²	1.3 10 ⁻²
perpflat	0.57 10 ⁻²	2.5 10 ⁻²	0.1 10 ⁻²
perpflat0#		1.6 10 ⁻²	

Non-Equilibrium Green Function - DFT calculations for transport properties

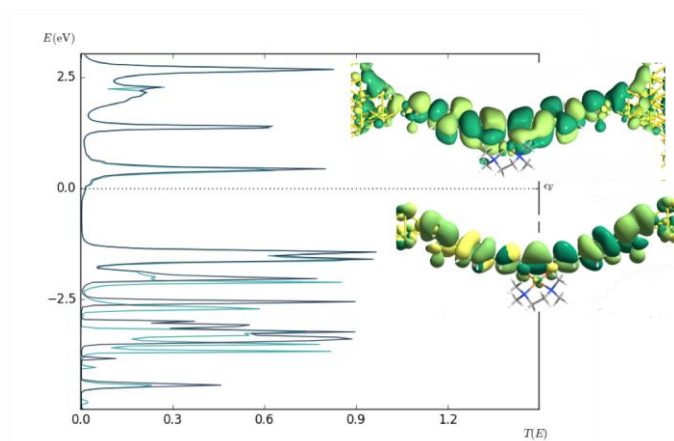


Figure S59. Transmission curves for the *flat0* conformer of MeS-CCM-Cu (**3**) calculated with the ATK code and PBE functional (green spin up, black spin down). The spin density of the Cu^{II} center is around 0.4 e⁻ (the empty beta $d_{x^2-y^2}$ orbital is above 3 eV out of the energy window). Transmission eigenfunctions were plotted for the frontier orbitals. The transmission eigenstates are obtained by diagonalizing the transmission matrix and the corresponding eigenvalues indicate the importance of each eigenstate in the transport. As it is a complex wavefunction, the color map indicating the phase of the function is represented from 0 to 2π by dark green to yellow colors. The value employed for the isosurface is 0.2.

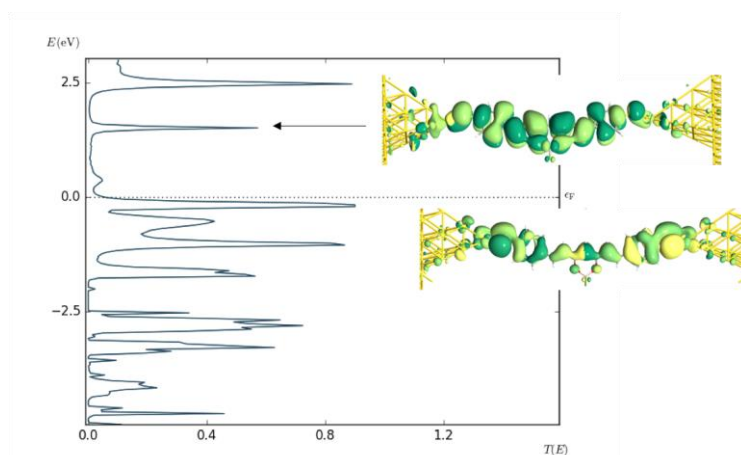


Figure S60. Transmission curves for S-CCM-BF₂ (**4**), assuming the formation of biradical due to the electrode interaction calculated with the ATK code and PBE functional. Transmission eigenfunctions were plotted for the frontier orbitals. The transmission eigenstates are obtained by diagonalizing the transmission matrix and the corresponding eigenvalues indicate the importance of each eigenstate in the transport. As it is a complex wavefunction, the color map indicating the phase of the function is represented from 0 to 2π by dark green to yellow colors. The isovalue employed for the isosurface is 0.2.

References

- 1 C. Ge, H. Wang, B. Zhang, J. Yao, X. Li, W. Feng, P. Zhou, Y. Wang, J. Fang, *Chemical Communications*, 2015, **51**, 14913.
- 2 D. W. Meek, S. A. Ehrhardt, *Inorganic Chemistry*, **1965**, 4, 584.
- 3 A. Etcheverry-Berríos, I. Olavarriá, M. L. Perrin, R. Díaz-Torres, D. Jullian, I. Ponce, J. H. Zagal, J. Pavez, S. O. Vásquez, H. S. J. van der Zant, D. Dulić, N. Aliaga-Alcalde, M. Soler, M., *Chemistry - A European Journal*, 2016, **22**, 12808.
- 4 C. A. Martin, R. H. M. Smit, R. Egmond, H. S. J. van der Zant, J. M. van Ruitenbeek, *Review of Scientific Instruments*, 2011, **82**, 053907.
- 5 C. A. Martin, J. M. van Ruitenbeek, H. S. J. van der Zant, *Nanotechnology*, 2010, **21**, 265201.
- 6 M. J. Frisch, G. W. Trucks, H. B. Schlegel, G. E. Scuseria, M. A. Robb, J. R. Cheeseman, G. Scalmani, V. Barone, B. Mennucci, G. A. Petersson, H. Nakatsuji, M. Caricato, X. Li, H. P. Hratchian, A. F. Izmaylov, J. Bloino, G. Zheng, J. L. Sonnenberg, M. Hada, M. Ehara, K. Toyota, R. Fukuda, J. Hasegawa, M. Ishida, T. Nakajima, Y. Honda, O. Kitao, H. Nakai, T. Vreven, J. A. Montgomery, J. E. Peralta, F. Ogliaro, M. Bearpark, J. J. Heyd, E. Brothers, K. N. Kudin, V. N. Staroverov, R. Kobayashi, J. Normand, K. Raghavachari, A. Rendell, J. C. Burant, S. S. Iyengar, J. Tomasi, M. Cossi, N. Rega, N. J. Millam, M. Klene, J. E. Knox, J. B. Cross, V. Bakken, C. Adamo, J. Jaramillo, R. Gomperts, R. E. Stratmann, O. Yazyev, A. J. Austin, R. Cammi, C. Pomelli, J. W. Ochterski, R. L. Martin, K. Morokuma, V. G. Zakrzewski, G. A. Voth, P. Salvador, J. J. Dannenberg, S. Dapprich, A. D. Daniels, Ö. Farkas, J. B. Foresman, J. V. Ortiz, J. Cioslowski, D. J. Fox, Gaussian 09 (Revision D.01), Wallingford, CT, 2009.
- 7 A. D. Becke, *Journal of Chemical Physics*, 1993, **98**, 5648.
- 8 M. Head-Gordon, J. A. Pople, M. J. Frisch, *Chemical Physics Letters*, 1988, **153**, 503.
- 9 S. Grimme, J. Antony, S. Ehrlich, H. Krieg, *The Journal of Chemical Physics*, 2010, **132**, 154104.
- 10 M. Saitow, U. Becker, C. Riplinger, E. F. Valeev, F. Neese, *The Journal of Chemical Physics*, 2017, **146**, 164105.
- 11 F. Neese, *Wiley Interdisciplinary Reviews Computational Molecular Science*, 2012, **2**, 73.
- 12 F. Weigend, R. Ahlrichs, *Physical Chemistry Chemical Physics*, 2005, **7**, 3297.
- 13 V. Blum, R. Gehrke, F. Hanke, P. Havu, V. Havu, X. G. Ren, K. Reuter, M. Scheffler, *Computer Physics Communications*, 2009, **180**, 2175.
- 14 J. P. Perdew, K. Burke, M. Ernzerhof, *Physical Review Letters*, 1996, **77**, 3865.
- 15 M. Brandbyge, J. L. Mozos, P. Ordejon, J. Taylor, K. Stokbro, *Physical Review B*, 2002, **65**, 165401.
- 16 M. Di Ventra, *Electrical transport in nanoscale systems*. Cambridge University Press: Cambridge, UK ; New York, 2008; p xvi, 476 p.
- 17 Atomistix ToolKit ATK, 2016.3; QuantumWise A/S: 2016.